JGR Atmospheres

RESEARCH ARTICLE
10.1029/2024JD043020

Diurnal Cycle of Summer Precipitation Over Mainland Southeast Asia Revealed by Observations, Reanalysis, and Dynamic Downscaling

Hui-Wen Lai[1], Tinghai Ou[1], Aiguo Dai[2], Xingchao Chen[3], and Aifang Chen[4]

[1]Department of Earth Sciences, University of Gothenburg, Gothenburg, Sweden, [2]Department of Atmospheric and Environmental Sciences, University at Albany, State University of New York, Albany, NY, USA, [3]Department of Meteorology and Atmospheric Sciences, and Center for Advanced Data Assimilation and Predictability Techniques, The Pennsylvania State University, University Park, PA, USA, [4]School of Environment and Civil Engineering, Dongguan University of Technology, Dongguan, China

Key Points:

- Observed summer precipitation diurnal cycles in mainland Southeast Asia are compared with dynamic downscaling at 3- and 9-km grid spacing driven by reanalysis
- Convective activity and near-surface winds influence the diurnal precipitation cycle, better captured by downscaling simulations than ERA5
- The 3-km simulation reduces ERA5's wet bias and outperforms the 9-km simulation in capturing precipitation frequency and intensity peaks

Supporting Information:

Supporting Information may be found in the online version of this article.

Correspondence to:

H.-W. Lai,
hui-wen.lai@gu.se

Citation:

Lai, H.-W., Ou, T., Dai, A., Chen, X., & Chen, A. (2025). Diurnal cycle of summer precipitation over mainland Southeast Asia revealed by observations, reanalysis, and dynamic downscaling. *Journal of Geophysical Research: Atmospheres*, *130*, e2024JD043020. https://doi.org/10.1029/2024JD043020

Received 21 NOV 2024
Accepted 15 MAY 2025

Author Contributions:

Conceptualization: Hui-Wen Lai
Data curation: Hui-Wen Lai, Tinghai Ou, Aifang Chen
Formal analysis: Hui-Wen Lai
Investigation: Aifang Chen
Methodology: Hui-Wen Lai, Tinghai Ou, Aiguo Dai, Xingchao Chen
Validation: Aiguo Dai
Visualization: Hui-Wen Lai, Xingchao Chen
Writing – original draft: Hui-Wen Lai
Writing – review & editing: Hui-Wen Lai, Tinghai Ou, Aiguo Dai, Xingchao Chen, Aifang Chen

Abstract The diurnal cycle of precipitation plays a crucial role in regulating Earth's water cycle, energy balance, and regional climate patterns. However, the diurnal precipitation across mainland Southeast Asia (MSEA) and the factors influencing its spatial variations are not fully understood. In this study, we investigated diurnal precipitation patterns in summertime (June–August) from 2002 to 2005 over MSEA using ground-based observations, satellite products, the global ERA5 reanalysis, and high-resolution simulations from the Weather Research and Forecasting (WRF) Model at 9- and 3-km grid spacing forced by ERA5 hourly data on ~0.25° grids. Various observation-based data sets including GHCN-Daily, Multi-Source Weighted-Ensemble Precipitation (MSWEP), Asian Precipitation - Highly-Resolved Observational Data Integration Towards Evaluation of Water Resources (APHRODITE), and Integrated Multi-satellite Retrievals for Global Precipitation Measurement (IMERG) were used. In evaluating daily precipitation over MSEA, MSWEP, and APHRODITE data sets show similar patterns in precipitation amount, frequency, and intensity, while IMERG tends to produce higher amounts but with less frequency. ERA5 overestimates light precipitation compared to the other data sets. The WRF simulations generally produce heavier but less frequent light precipitation, with the 3-km simulation producing less intense precipitation than the 9-km simulation. A k-means classification of IMERG data revealed five distinct spatial regimes with varying diurnal precipitation cycles. The WRF simulations closely match these regimes, capturing key diurnal cycles missed by ERA5 over mountainous regions and coastlines. Additionally, convective activities and near-surface winds influence these cycles, with WRF simulations better representing coastal and mountain precipitation patterns than ERA5. High-resolution WRF simulations, especially the 3-km simulation, capture diurnal precipitation more accurately than ERA5, highlighting the importance of employing convection-permitting models to simulate precipitation diurnal cycles over complex terrain.

Plain Language Summary This study examines the daily precipitation patterns (diurnal cycles) across mainland Southeast Asia (MSEA), a region that heavily relies on rainfall for agriculture and water resources. Understanding these patterns is crucial as the region faces increasing drought risks due to climate change. The research highlights differences between data sets and models. High-resolution Weather Research and Forecasting (WRF) simulations more accurately capture precipitation timing and intensity, particularly in complex terrains like mountains and coastlines, than the widely used ERA5 data set. While ERA5 often shows precipitation peaks earlier in the day and misses late-night and morning rainfall, WRF models closely align with satellite data (Integrated Multi-satellite Retrievals for Global Precipitation Measurement), identifying distinct rainfall regimes across the region. The study also shows that the differences in precipitation among modeling data sets are due to simulated near-surface winds and convective activities. These findings indicate the importance of using high-resolution models to understand precipitation variability in MSEA. The results provide insights for improving models and developing strategies to address water resource management and agricultural challenges under a changing climate.

1. Introduction

The diurnal cycles of convective activity and precipitation play important roles in the energy and water cycles, especially in the low latitudes. These cycles could account for more than 50% (25%) of the precipitation diurnal

amplitudes over land (ocean) in the tropics (Watters et al., 2021). Mainland Southeast Asia (MSEA), one of the major crop-growing regions in the tropics (Kuenzer & Knauer, 2013), has experienced ongoing challenges related to drought risk, and models project increased drought risk in the region in the near future (L. Zhang et al., 2021). The diurnal timing of precipitation can have a large impact on surface evaporation and thus soil moisture. Thus, an improved understanding of the precipitation diurnal cycle over MSEA is essential for understanding precipitation variability and its impact on land surface conditions in this region.

There are several areas with mountainous topography in MSEA, and the complex terrain can modulate the diurnal cycle of precipitation spatially. Typically, convection tends to occur in the late afternoon or evening over most land areas (Dai et al., 2007). In MSEA, rainfall peaks have often been observed in the early afternoon over the mountain ranges, in the evening in the valleys, and in the afternoon (night) on land (ocean) along the coastlines (P. Chen et al., 2024; Ohsawa et al., 2001). In addition, a precipitation pattern of late-night-early-morning peaks has been observed on the eastern Khorat Plateau, which is related to the eastward propagation of diurnal rainfall systems (Satomura, 2000). In the study area, the production of diurnal precipitation is mainly influenced by solar insolation, mountain-valley breezes, land-sea contrast, and low-level convergence (Biasutti et al., 2012; Kim et al., 2019; Tsujimoto et al., 2018; Yang & Slingo, 2001). Most previous studies using observations and/or model simulations have focused on the diurnal cycles of precipitation over predefined regions of MSEA. As a result, there is a notable gap in understanding the broader spatial patterns of diurnal precipitation and related atmospheric variables across MSEA.

Due to the complex topography and scarcity of observations in certain regions, high-resolution observation, such as radar and satellite, and atmospheric modeling become crucial for investigating the precipitation patterns and the impacts of the topography in these regions. Spaceborne radars better capture the magnitude and the phase of diurnal precipitation (L. Hayden & Liu, 2021), but its coverage is limited in both space and time. In contrast, passive microwave observations offer broader spatiotemporal coverage but are known to exhibit variable time lags over convective regions (L. Hayden & Liu, 2021). Regional climate models (RCMs) have been widely used to study precipitation in MSEA. Several studies have demonstrated that RCMs capture reasonable precipitation patterns (Tangang et al., 2019) and interannual variability (Khiem et al., 2014) over MSEA. Increases in the spatial resolutions of models (up to about 10 km) have primarily enhanced the amplitude of the diurnal precipitation compared to observations but had limited impacts on the timing of rainfall (Dirmeyer et al., 2012) and may introduce larger bias over the elevated terrain (Kim et al., 2019). When increasing the model resolution to smaller than 10 km, modelers typically turn off the convection scheme in the simulations, which often results in more accurately simulated peak precipitation (M. Chan et al., 2022; L. J. M. Hayden et al., 2023; Ou et al., 2020). Although RCMs can better reproduce the spatial distributions of precipitation than the driving global climate models (GCMs), they tend to overestimate the amount of precipitation (Nguyen et al., 2022). Previous studies have shown that simulations with coarse resolutions or even mesoscale grids have a “drizzling” bias, which results in too much light rain (D. Chen et al., 2021; Zhou et al., 2022). The use of cumulus parameterization in global or regional models could also be an issue affecting the performance of diurnal cycles (Liang et al., 2004; Z. Liu et al., 2022; Tao et al., 2024). In addition, it is challenging for RCMs to capture the precipitation intensity, especially for extreme events (e.g., Hariadi et al., 2023; Nguyen et al., 2022). Despite the advancements from GCMs to RCMs, notable biases and uncertainties persist in the simulation results. Therefore, higher-resolution modeling than conventional RCMs needs to be explored (Chung et al., 2023; Tangang et al., 2021).

Recent studies have revealed that high-resolution simulations from the Coordinated Regional Climate Downscaling Experiment (CORDEX)-SEA Phase 2, which has a 5-km horizontal spacing, reduced precipitation biases compared with CORDEX-SEA phase 1, which has a 25 km spacing (Chung et al., 2023). Convection-permitting models (CPMs) with a model grid spacing of about 4 km or less have been demonstrated to reduce the wet biases in the fifth-generation European Centre for Medium-Range Weather Forecasts (ECMWF) atmospheric reanalysis (ERA5) over complex regions because they resolve the topography better (Lin et al., 2018). Other examples have shown that CPMs can better represent the peak time and amount of diurnal precipitation induced by local circulation over Northeastern Thailand (Takayabu et al., 2021) and the northern and southern parts of MSEA (Jones et al., 2023; Xiang et al., 2024). Over the Tibetan Plateau, where the mountain ranges extend to the northern part of Southeast Asia (SEA), applying a CPM could reduce the overestimation of the precipitation produced by lower resolution models and could better capture the observed diurnal cycles of the precipitation in the mountainous regions (e.g., P. Li et al., 2021; Z. Liu et al., 2022). Despite the advantages of using CPMs in precipitation simulations, the impact of the horizontal grid spacing on the modeling improvement has not been examined over

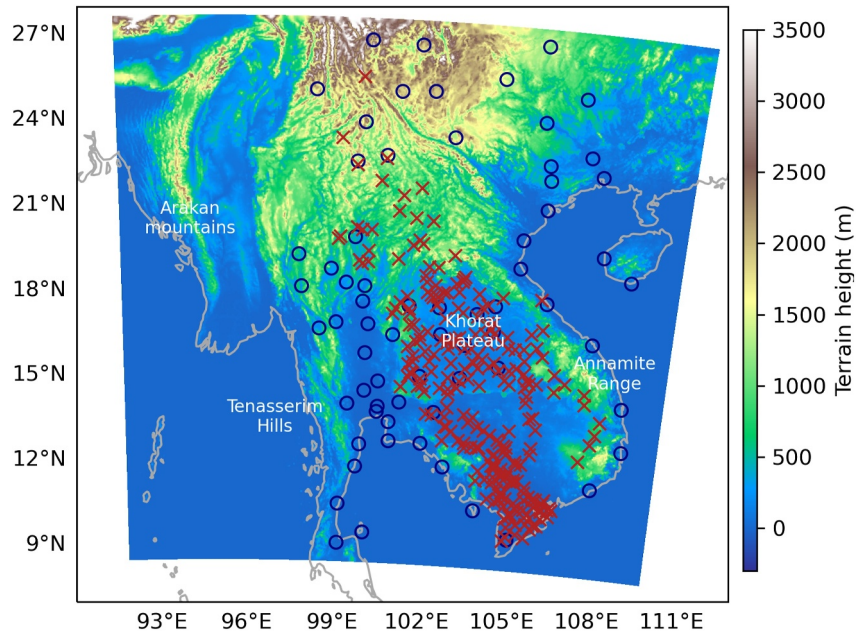

Figure 1. Map of the study area in mainland Southeast Asia and locations of the in situ observation stations used. The blue circles denote the GHCN-Daily stations, and the red x symbols denote the stations used by Wang et al. (2016). Color shading indicates the elevation.

the entire MSEA (Ferrett et al., 2021). Few studies have focused on the use of CPMs in precipitation research within local regions in MSEA, and the overall performances of CPMs in simulating diurnal precipitation across MSEA and the associated underlying processes remain unclear.

In this study, we attempt to systematically study the diurnal cycle of precipitation across MSEA and the related physical processes in high-resolution atmospheric simulations by producing the first CPM data set for this region. Specifically, we aim to (a) explore the spatial distributions of different precipitation diurnal cycle regimes over MSEA, (b) evaluate the precipitation simulated by a dynamic downscaling at 9- and-3 km grid spacing driven by reanalysis, and (c) investigate the underlying physical processes behind the differences in the simulated precipitation.

2. Data and Methods

In this study, we focused on the summertime (June-July-August or JJA)) precipitation during 2002–2005 within MSEA (Figure 1) due to the availability of abundant in situ observations during this period compared to other years. Additionally, we examined the diurnal cycles of precipitation for the 2002–2005 and 2015–2018 and found small differences in the timing of precipitation peaks, which is the primary focus of this study (Figure S1 in Supporting Information S1). The elevation ranges from 0 to 4,860 m for MSEA, and the higher mountains extend from the southeastern corner of the Tibetan Plateau (Figure 1). Summer precipitation within this region is mainly influenced by monsoons and the local topography. We applied the local solar time (LST) to investigate the diurnal cycles. The studied area is between 92° and 110°E with 101°E as the center of the domain; therefore, we used UTC+7 as the LST for the entire study region.

2.1. ERA5

The ERA5 data set provides hourly estimates of atmospheric variables globally and has a horizontal grid spacing of approximately 31 km (Hersbach et al., 2020). We used hourly total precipitation data on a $0.25° \times 0.25°$ grid for 2002–2005. Note that the total precipitation in ERA5 was forecasted from the 06 and 18 UTC analyses, rather than derived from the analysis data (ECMWF, n.d.). The following variables were also used to investigate the precipitation processes: the convective available potential energy (CAPE), boundary layer height (BLH), mean

surface sensible heat flux (SHF), mean surface latent heat flux (LHF), 10-m u component of the wind (U10), and 10-m v component of the wind (V10).

2.2. In Situ Observations

The Global Historical Climatology Network data set was used as a reference for the model validations conducted in the study. The GHCN-Daily (GHCN-D) data set is a comprehensive repository of historical daily data from weather stations (Menne et al., 2012). We selected JJA precipitation data for 2002–2005 over MSEA from the GHCN-D. Stations with ≥50% sampling rates during JJA from 2002 to 2005 are used, which results in a total of 67 stations (circles in Figure 1).

Another in situ precipitation data set used here was obtained from Wang et al. (2016). This data set is a compilation of data from rain gauges located around the Mekong River Basin. The two data sets (GHCN-D and Wang et al., 2016) were applied together to evaluate the daily precipitation data from the other data sets and models used in the study. To avoid overlaps between these two data sets, we removed stations that were located less than 10 km from another station. We also filtered out the station data with lower sampling rates with a recording time range of <50%. After this, the number of stations from Wang et al. (2016) included in this study was 247 (x symbols in Figure 1) during JJA 2002–2005.

2.3. Gridded Observations

In addition to in situ station observations, we also used gridded observations, which provide better spatial coverage over the entire study area, for the precipitation evaluation. The Asian Precipitation - Highly-Resolved Observational Data Integration Towards Evaluation of Water Resources (APHRODITE) project offers a compilation of observational data of daily precipitation and other variables across Asia (Yatagai et al., 2012). It also satisfactorily represents the precipitation observed by gauges in the study area (Tian et al., 2021). Daily precipitation data for JJA during 2002–2005 from the APHRO_MA V1901 version precipitation data set for the monsoon Asia domain on 0.25° grids were used here. Because there is a 0.125° shifting in both latitudes and longitudes between the grids of ERA5 and APHRODITE, we remapped the APHRODITE data onto ERA5 grids using linear interpolation.

We also used the Integrated Multi-satellite Retrievals for Global Precipitation Measurement (IMERG) version 06B data set derived from satellite observations. The IMERG provides highly detailed information about global precipitation patterns (Huffman et al., 2020) and spatiotemporal patterns of diurnal precipitation similar to those observed by the Ku radar observation (L. J. M. Hayden et al., 2023). However, the IMERG precipitation mainly captured the diurnal cycle of convective precipitation that peaks a few hours later than surface-observed precipitation (Dai, 2024), a common feature in satellite data sets (Dai et al., 2007). We applied the half-hourly precipitation data from the IMERG version V06B product on 0.1° grids for JJA during 2002–2005. The data from IMERG were mainly used to conduct the daily and hourly precipitation evaluations.

Another gridded observational precipitation data set, the Multi-Source Weighted-Ensemble Precipitation (MSWEP, Beck et al., 2019), is also applied for the subdaily precipitation evaluation. The MSWEP product includes precipitation data from gauge observation, satellites, and reanalyses (Beck et al., 2019). It has been suggested that the diurnal phase of MSWEP is slightly earlier than other satellite-based data sets and the amplitude of diurnal precipitation is smaller than IMERG (Dong et al., 2023). MSWEP has also been reported to produce earlier peaks in precipitation amount than radar observation in the Amazon Basin (Sapucci et al., 2022), which could be used as a reference to examine the late peaks of diurnal precipitation from IMERG. The data set provides a 3-hourly output with 0.1° grid spacing. We used its subdaily precipitation for JJA during 2002–2005 over MSEA.

For wind comparison, we used 10-m surface winds from the cross-calibrated multiplatform (CCMP) project, produced by remote sensing systems. CCMP integrates 10-m ocean surface wind from various satellite observations with ERA5 10-m winds as the background field. We used 6-hourly wind data from the version 3.1 product on 0.25° grids for JJA from 2002 to 2005.

2.4. WRF Model Configuration

High-resolution and convection-permitting simulations were conducted using the Weather Research and Forecasting (WRF) Model version 3.7.1 (Skamarock et al., 2008). Two simulations were conducted with a horizontal grid spacing of 9 and 3 km for the period from 1998 to 2018 with an additional 1-year spin-up period, and the two simulations were connected through one-way nesting. The simulations incorporated the following physical parameterizations. The double-moment 6-class scheme (WDM6; Lim & Hong, 2010) was employed for cloud microphysics, due to its better performance in simulating warmer-type heavy rain than other microphysics schemes (Chakraborty et al., 2021; H.-J. Song & Sohn, 2018). For land surface and planetary boundary layer processes, the Noah land surface model and the Yonsei University schemes (Hong et al., 2006) were used, respectively. The new Goddard shortwave radiation and the rapid radiative transfer model for general circulation model long-wave radiation were utilized for the atmospheric radiation processes (Iacono et al., 2008; Matsui et al., 2020), following X. Chen et al. (2018), which has shown that this combination can well capture the salient features of Indian summer monsoon. Gray-zone resolutions (e.g., 9 km) improve convective process representation by explicitly resolving convection (i.e., no cumulus parameterization), reducing parameterization errors, and enhancing model performance in some regions (X. Chen et al., 2018; Ou et al., 2020). However, they can also lead to precipitation overestimation (Park et al., 2022). Ou et al. (2020) found that precipitation diurnal cycles, especially in precipitation amount and frequency, could be better captured in simulations at 9-km grid spacing without a convection scheme, in a region upstream of our study domain. Given their findings, we followed this approach and conducted the 9- and 3-km simulations without using cumulus parameterization. The initial and boundary conditions for these simulations were derived from the ERA5 hourly data on 0.25° grids. The WRF model utilized 60 terrain-following vertical layers, and the top of the model was located at 10 hPa. These 9-km and 3-km simulations are referred to as WRF9 and WRF3. The WRF9 domain covers East and South Asia (Ou et al., 2023), while WRF3 is nested to WRF9 where the domain covers MSEA. The WRF simulations with 9-km grid spacing have been shown to reduce the wet bias in ERA5 precipitation over the Tibetan Plateau (Ou et al., 2023).

2.5. Diurnal Cycles

To evaluate the performance of the WRF simulations, we computed the hourly precipitation amount, intensity, and frequency using hourly precipitation from ERA5 and IMERG data sets and WRF output. The hourly precipitation amount is defined as the average of the accumulated precipitation amount during each hour over a given period (i.e., JJA from 2002 to 2005) including nonprecipitating days. The precipitation frequency for a given hour of day is defined as the percentage of days when precipitation is 0.1 mm hr^{-1} or higher during that hour. The precipitation intensity is defined as the average precipitation amount for the given hour over days when precipitation is 0.1 mm hr^{-1} or higher for the hour. For daily precipitation frequency and intensity calculations, the precipitation threshold is 2.4 mm day^{-1} derived from 24 hr x hourly threshold of 0.1 mm.

To minimize the impact of data resolution (D. Chen & Dai, 2018), precipitation data from IMERG and WRF were averaged to the 0.25° (~31 km) grids of ERA5 by simply averaging the precipitation over the finer grid boxes that were close to an ERA5 coarser grid box. The averaged areas for IMERG, MSWEP, and WRF9 output were 3×3 grids while the averaged areas for WRF3 output were 9×9 grids. Such simple averaging was recommended over spatial interpolation by D. Chen and Dai (2018) to minimize the alteration of precipitation frequency and intensity by the remapping. This averaged precipitation data on ERA5 grids were applied to the k-means classification (Sections 2.6 and 3.1) and precipitation evaluations (Section 3.2). The precipitation data used in the k-means classification were hourly precipitation as a percentage of daily precipitation averaged over four summers (2002–2005) and calculated for each grid box at the given hour. The k-means classification reveals the primary mode of the diurnal cycle in precipitation at each grid box.

2.6. k-Means Classification

k-means classification is an unsupervised machine learning algorithm that has been widely used for data analysis and pattern recognition in the field of atmospheric science. This algorithm classifies a data set into distinct groups or clusters based on similarities in their features. In atmospheric science, k-means classification has been utilized to categorize weather patterns and to identify similarities and differences in atmospheric variables (e.g., Curio & Scherer, 2016; Schubert et al., 2017). We applied k-means training to the diurnal cycles of normalized hourly

precipitation (in a percentage of the daily mean, Section 2.5) from regridded IMERG (onto ERA5 grids) for JJA from 2002 to 2005. The hourly precipitation data were averaged over the four summers to reduce its interannual variations. Therefore, the sample size for the k-means classification was the number of grid points over the analysis domain (i.e., MSEA). To obtain the optimal k-means size for classification, we conducted clustering across a range of cluster sizes and calculated the mean Euclidean distance between the input data points and their corresponding closest k-means clusters. After testing cluster numbers of 1–20, we determined that five clusters were sufficient to capture the variability of the hourly precipitation data (Figure S2 in Supporting Information S1). After this, the five-cluster k-means model trained with IMERG precipitation, which identifies five different diurnal regimes (Figure 5e), was employed to classify the 4-year averaged diurnal cycles of precipitation from IMERG, ERA5, and two WRF simulations in terms of where each of the five diurnal regimes may occur in each data set.

3. Results and Discussion

3.1. Evaluation of Daily and Subdaily Precipitation From the Model Simulations

Given the restricted availability of hourly precipitation observations over MSEA, our evaluation focused on the daily precipitation patterns in regions with distinct diurnal cycles of precipitation. Figure 2 shows the daily precipitation amount, frequency, and intensity from several observational data sets and the WRF9 and WRF3 simulations. Most precipitation occurs along the Annamite Range in eastern MSEA and on the windward slopes of the Tenasserim Hills and Arakan Mountains in western MSEA (Figures 2a1–2a7). In situ station observations show less precipitation amount than the other products, which could be caused by missing data on some days and specific geographic locations between the monitoring stations and gridded data sets Figures 2a1–2a7. Precipitation amounts from APHRODITE and MSWEP suggest similar patterns, with high precipitation along the western coastlines and eastern mountain regions, while lower precipitation occurs in the western inland areas of MSEA (Figures 2a2 and 2a3). In contrast, IMERG shows generally higher precipitation amounts in areas where APHRODITE and MSWEP indicate lower precipitation (Figures 2a2–2a4). On the other hand, ERA5 suggests higher precipitation in the western inland and northern regions of MSEA, which is similar to IMERG. The two WRF simulations show lower precipitation amounts in most regions than the other data sets, with WRF3 showing even lower precipitation amounts than WRF9.

The spatial patterns of precipitation frequency are similar to the precipitation amount, with areas of higher precipitation amount generally experiencing more frequent precipitation. Among the data sets, APHRODITE, MSWEP, and ERA5 tend to produce higher precipitation frequencies across the region while IMERG and the two WRF simulations show lower frequencies (Figures 2b2–2b7). When examining precipitation intensity, APHRODITE, MSWEP, and ERA5 exhibit lighter precipitation (Figures 2c2, 2c3, and 2c5). The IMERG and two WRF products suggest stronger precipitation intensity, especially in the western coastline and the eastern mountain regions (Figures 2c4, 2c6, and 2c7). Because precipitation frequency (intensity) increases (decreases) with the size of the averaging area (D. Chen & Dai, 2018), it is expected that the unaveraged station data, which cover the smallest area, should have the lowest overall frequency (Figure 2b1) but high intensity (Figure 2c1), especially over the eastern MSEA. Overall, APHRODITE, MSWEP, and ERA5 show similar spatial patterns in precipitation amount, frequency, and intensity. On the other hand, the WRF9 simulations produce the least frequent precipitation but the highest intensity among all the data sets, while WRF3 and IMERG show similar precipitation frequency and intensity patterns.

Next, we examined the histograms of daily precipitation over MSEA (Figure 3). Precipitation frequencies from APHRODITE and MSWEP agree with each other below 60 mm day^{-1} and above 220 mm day^{-1}, while APHRODITE suggests less frequency of heavy precipitation (60–220 mm day^{-1}) (Figures 3a and 3b). Precipitation frequency from IMERG is less than APHRODITE and MSWEP for intensity below 45 mm day^{-1} and higher for intensity above 45 mm day^{-1}. This agrees with previous studies, which have shown that MSWEP and APHRODITE produce generally well precipitation patterns compared with gauge-based data among gridded precipitation products (Dangol et al., 2022; Elahi et al., 2024), while IMERG can sometimes perform better than MSWEP and APHRODITE (e.g., Gupta et al., 2024; Tran et al., 2023).

The occurrences of different precipitation intensities are similar between ERA5 and MSWEP for light precipitation (below 100 mm day^{-1}). However, the ERA5 has a higher frequency of heavy precipitation and follows a pattern closer to IMERG for precipitation in the 100–300-mm day^{-1} range. In general, the frequency of ERA5 heavy precipitation (>100 mm day^{-1}) falls between the observation-based data sets (APHRODITE, MSWEP,

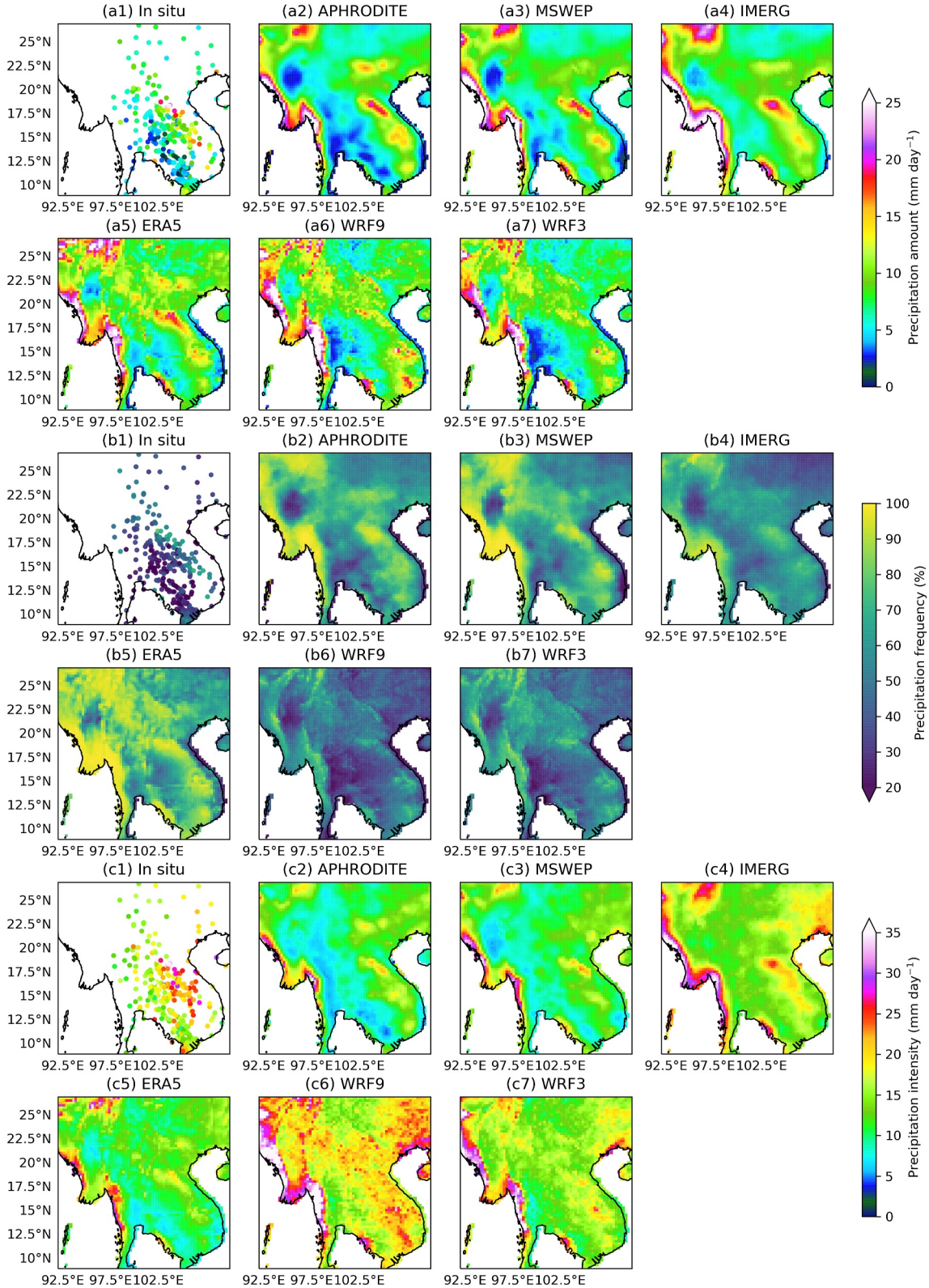

Figure 2.

and IMERG). On the other hand, ERA5 overestimates light precipitation (<30 mm day^{-1}; Figure 3b), which could be related to the "drizzling" bias caused by the cumulus parameterization scheme (D. Chen & Dai, 2019). The precipitation histograms derived from the WRF3 simulations and IMERG show close alignment for intensities up to 100 mm day^{-1}. Both WRF3 and WRF9 simulations overestimate the frequency of heavy precipitation above 100 mm day^{-1} compared to IMERG, while WRF9 also produces the highest daily precipitation between 30 and 420 mm day^{-1} (Figures 3a and 3b). In general, the WRF3 simulations reduce the wet bias for lighter rainfall (<30 mm day^{-1}) in ERA5, generate less heavy precipitation than WRF9, and produce an intensity-frequency curve closer to IMERG. In this case, the CPM (WRF3) simulations can reproduce the observed precipitation histograms better, particularly for light and heavy precipitation compared with RCM (WRF9).

Overall, Figures 3a and 3b show that the histograms of ERA5 daily precipitation are more consistent with those of APHORDITE, MSWEP, and IMERG than with the WRF simulations, suggesting that ERA5 daily precipitation is realistic, while the two WRF simulations tend to overestimate heavy precipitation compared with APHORDITE and MSWEP. IMERG and the two WRF simulations tend to overestimate heavy precipitation over MSEA during summer, although the CPM simulations (WRF3) show some improvements over the non-CPM simulations (WRF9).

To evaluate the precipitation simulations for different elevations, we compared the bias of the daily precipitation using MSWEP as a reference. The median of biases from APHRODITE and IMERG are close to zero at all the elevation bins while IMERG shows less interquartile range than APHRODITE (Figure 3c). The ERA5 tends to overestimate precipitation at all elevations. The WRF simulations have smaller biases or a dry bias than ERA5. The mean biases of the WRF9 and WRF3 are not obviously different, but the WRF3 has an overall smaller bias and less variation than WRF9 at all the elevation bins.

Based on MSWEP and IMERG data, the average diurnal precipitation cycle in MSEA shows a large peak in precipitation amount during the afternoon and a smaller peak around midnight (black solid and gray dashed lines in Figure 4a). A peak of precipitation frequency is also in the afternoon, while high precipitation intensity occurs in both the early-morning and afternoon (black solid and gray dashed lines in Figures 4b and 4c). A comparison of the averaged diurnal cycles of precipitation indicates that MSWEP and IMERG show similar peak timing in precipitation frequency and intensity but with apparent differences in their magnitudes (Figures 4b and 4c). For precipitation amount, the magnitudes from MSWEP and IMERG are similar, but IMERG shows a later peak (Figure 4a). This could be due to the known issue in IMERG that has a delayed peak by a few hours when compared with surface observations (Dai, 2024; R. Li et al., 2018). The ERA5 tends to overestimate precipitation amounts compared to the other gridded data sets (Figure 4a). In contrast, the two WRF simulations align more closely with the MSWEP product in terms of magnitudes and timing of the peaks. For precipitation frequency, ERA5 shows a high precipitation frequency (40%) from morning to early afternoon while MSWEP also shows a high frequency later (Figure 4b). On the other hand, IMERG and the two WRF simulations show increased precipitation frequency after 1200 LST close to MSWEP but with a lower frequency (below 30%) (Figure 6b). Lastly, the MSWEP and IMERG data sets show higher precipitation intensity from late evening to early morning, in contrast to the peak intensity occurring in the early afternoon in ERA5 (Figure 4c). The diurnal cycles of precipitation intensity from the two WRF simulations follow more closely with IMERG, though with a positive bias.

In the 3-hourly precipitation comparison, ERA5 shows close values in precipitation amount, frequency, and intensity to the MSWEP. However, the timing of the frequency and intensity peaks are different from those of MSWEP and the other data sets. The patterns of the two WRF simulations are generally closer to IMERG than others in terms of peak timing and magnitudes. This difference highlights the tendency of the IMERG and the two WRF data sets to underestimate (overestimate) the precipitation frequency (intensity). This finding is consistent with previous studies showing that CPM produces more intense precipitation and less frequent light rain than IMERG (Jones et al., 2023). On the other hand, WRF3 outperforms WRF9 in simulating the amount, frequency, and intensity of precipitation cycles, especially in the magnitudes.

Figure 2. Spatial distribution of precipitation (a1–a7) amount (mm day^{-1}), (b1–b7) frequency (%), and (c1–c7) intensity (mm day^{-1}) derived from daily precipitation during June-July-August 2002–2005. Numbers 1–7 represent precipitation products from in situ station observation, Asian Precipitation - Highly-Resolved Observational Data Integration Towards Evaluation of Water Resources, Multi-Source Weighted-Ensemble Precipitation, Integrated Multi-Satellite Retrievals for Global Precipitation Measurement, ERA5, WRF9, and WRF3. All daily precipitation data were averaged onto the ERA5 grids before calculating the amount, frequency, and intensity. Note that the temporal coverage of in situ observation is less than that of other data sets due to missing data on some days.

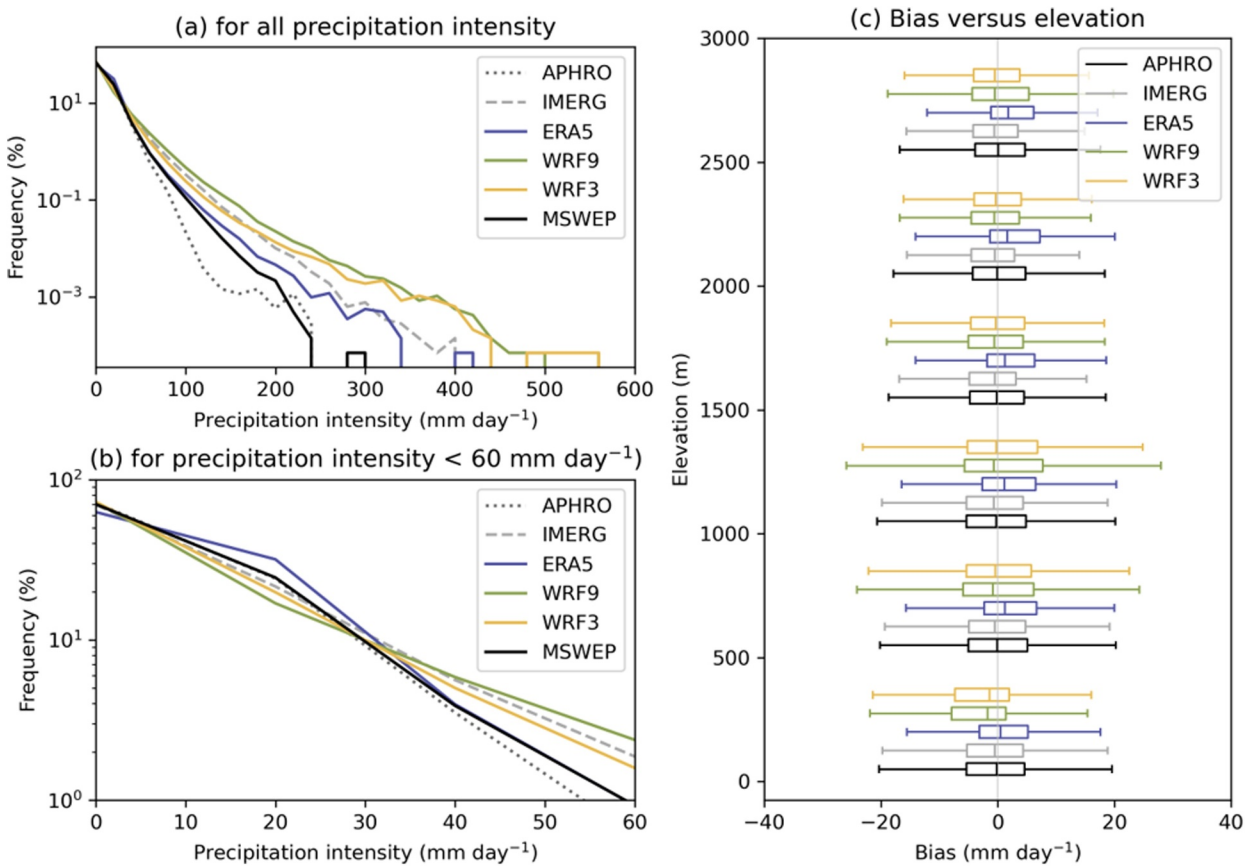

Figure 3. Histograms of (a) all daily precipitation (bin size = 20 mm day^{-1}) and (b) daily precipitation lighter than 60 mm day^{-1} (bin size = 20 mm day^{-1}) from Asian Precipitation - Highly-Resolved Observational Data Integration Toward Evaluation of Water Resources (APHRODITE) (dotted), Integrated Multi-Satellite Retrievals for Global Precipitation Measurement (IMERG) (dashed), ERA5 (blue), WRF9 (green), WRF3 (yellow), and Multi-Source Weighted-Ensemble Precipitation (MSWEP) (solid black) over the mainland Southeast Asia (MSEA) land surface in June-July-August (JJA) from 2002 to 2005. (c) Elevation-dependent biases (relative to MSWEP) in daily precipitation amount from APHRODITE (black), IMERG (gray), ERA5 (blue), WRF9 (green), and WRF3 (yellow) over the MSEA land surface for JJA from 2002 to 2005. All the daily precipitation data were averaged onto the ERA5 0.25° grids from which the histograms were derived by taking the daily precipitation at each grid as one data point.

3.2. Spatial Distributions of the Precipitation Diurnal Cycle Over MSEA

The k-means classification suggests a total of five distinct regimes of the diurnal variations in normalized hourly precipitation (in percentage of daily mean) based on the IMERG data set (Figures 5a and 5e). These distinct regimes reveal that precipitation diurnal peaks occur at different times of day in various regions: late night (peak

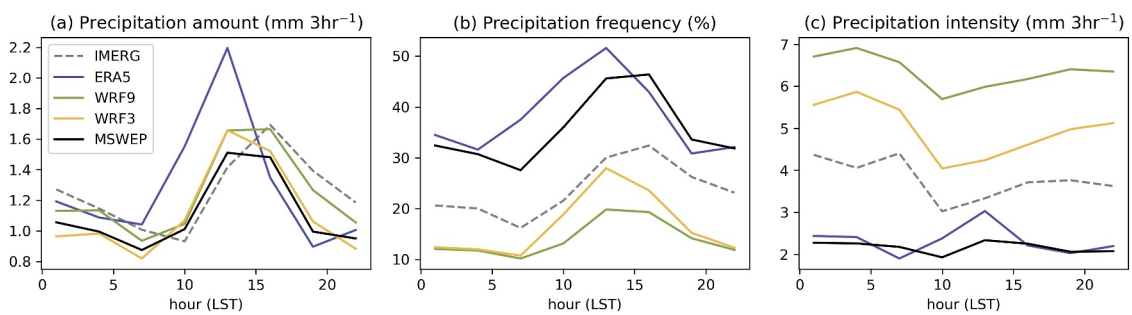

Figure 4. The diurnal cycle of 3-hr accumulated precipitation (a) amount, (b) frequency, and (c) intensity averaged over the land surface of mainland Southeast Asia from Multi-Source Weighted-Ensemble Precipitation (solid black), Integrated Multi-Satellite Retrievals for Global Precipitation Measurement (dashed gray), ERA5 (blue), WRF9 (green), and WRF3 (yellow) data sets in June-July-August during 2002–2005. All the precipitation data were processed to 3-hourly accumulations and averaged onto the ERA5 0.25° grids before the analysis.

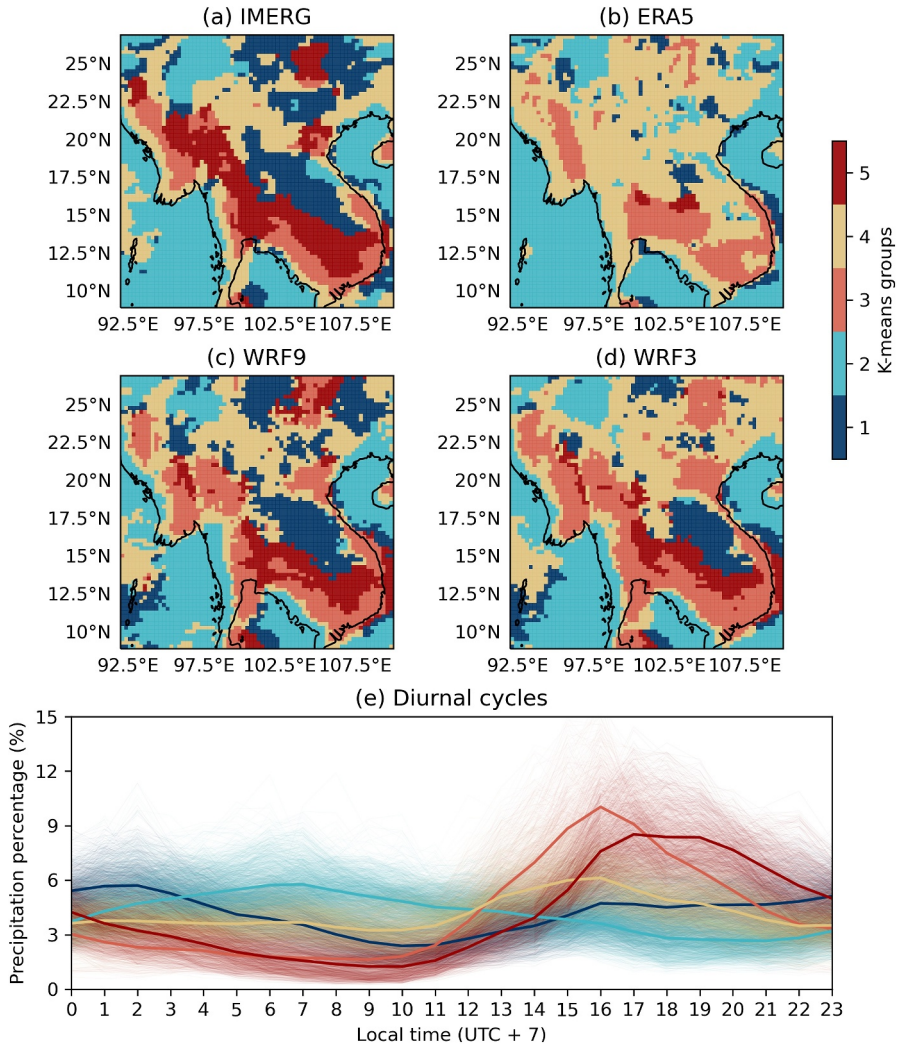

Figure 5. Distributions of the primary groups over mainland Southeast Asia from the k-means classification of the precipitation (in percentage of the daily mean) from (a) Integrated Multi-Satellite Retrievals for Global Precipitation Measurement (IMERG), (b) ERA5, (c) WRF9, and (d) WRF3 for June-July-August averaged over 2002–2005. (e) The mean diurnal cycle of the normalized precipitation (in percentage of the daily mean) average over the areas of the individual k-means groups (thick lines) and the diurnal cycle at individual grid boxes of each group (thin lines with the same color as the thick lines) based on the IMERG data. The same groups of (e) were applied to the other three data sets to reveal their distributions shown in (b–d).

around 02 LST, Group 1), morning (peak around 07 LST, Group 2), afternoon (a higher peak around 16 LST, Group 3 and a lower peak around 16 LST, Group 4), and evening (peak around 17–19 LST, Group 5; Figure 5e). The western coastlines of MSEA are classified as the morning regimes, and most of the inland area is classified as the afternoon and evening regimes. The eastern Khorat Plateau and the mountainous area close to the eastern Tibetan Plateau are classified as the late-night regime. The northern part of the Annamite range and northern Myanmar are classified as the morning regime. This comprehensive classification provides insights into the spatial distribution in the precipitation diurnal cycle over MSEA, thus providing a better understanding of the regional precipitation diurnal characteristics.

The classification of ERA5 precipitation based on the five regimes trained using the IMERG data reveals the afternoon regimes (the lower peak regime) around 16 LST over most MSEA, while the IMERG classification shows an evening precipitation peak around 18 LST across the central MSEA (Figures 5a and 5b). This phase difference is consistent with the results found by Dai (2024), who suggested that IMERG, like other satellite products, tends to mainly capture the diurnal cycle of convective precipitation, which lags the phase of total

precipitation by a few hours (Dai et al., 2007). However, an earlier peak in ERA5 does not necessarily indicate better accuracy. The previous comparison with MSWEP, which includes precipitation from rain gauges, satellites, and reanalyses, suggests that ERA5 peaks too early (Figure 4a). In the eastern and northern MSEA, evening, late-night, and morning peaks occur in IMERG, while ERA5 suggests the occurrence of lower afternoon or morning peaks. In addition, ERA5 fails to capture the late-night regime in the eastern Khorat Plateau. Overall, ERA5 simulated precipitation peaks at an earlier time over MSEA than the satellite observations from IMERG, which is known to have a delayed peak by a couple of hours when compared with surface observations reported not only for MSEA but also for other regions (Dai, 2024; L. J. M. Hayden et al., 2023; R. Li et al., 2018). The classification results from WRF9 and WRF3 demonstrate that high-resolution modeling can capture the spatial patterns of the different precipitation diurnal regimes, which closely align with the IMERG data. The results of the WRF3 are similar to those of the WRF9, except the fact that there are more afternoon regimes (groups 3 and 4) than the evening regime (Group 5) from central to northern MSEA.

Next, we investigated the precise peak times within the diurnal cycles for the data sets that provide hourly output. Figure 6 shows that the WRF simulations capture the diurnal peak timing more aligned with IMERG than ERA5. These differences in the peaks of precipitation amount are consistent with those shown in Figures 4a and 5. In addition, ERA5 captures the precipitation peaks of frequency in the morning for the mountainous regions (the late-night regime) while the other data sets produce afternoon–late-night peaks. This could be one of the reasons that ERA5 shows an earlier peak of precipitation frequency when averaging over the entire MSEA land surface (Figure 4b). Regarding the peak time of precipitation intensity, IMERG and the two WRF simulations produce the peak between evening and morning for most of the areas while ERA5 produces most peaks from noon to afternoon. Overall, the afternoon peaks of the precipitation amount, frequency, and intensity in ERA5 occur much earlier (about 2–5 hr) than IMERG over the majority of MSEA (Figures 6a2–6c2, 6a5–6c5). Although IMERG tends to delay the peak in precipitation amount, its peak timing in frequency and intensity aligns well with MSWEP, which tends to peak earlier (Figures 4b and 4c). Therefore, the two WRF simulations, which closely match IMERG, likely better capture precipitation frequency and intensity peaks than ERA5, which produces the earliest peaks among all studied data sets in the region (Figures 6b6–6b7, 6c6–6c7). We also found that WRF3 produces earlier peaks in precipitation amount and frequency than WRF9. This is especially true for the evening and late-night regimes.

Regarding the differences in peak timing among the modeling products, the tendency for earlier diurnal precipitation is shown not only in ERA5 but also in other RCMs and CMIP6 high-resolution models with a grid spacing of around 25 km (e.g., J. Song et al., 2024). As grid spacing decreases from 25 to 9 km, the error in the peak time seems reduced in which the peak time tends to move from an earlier peak to a later peak (e.g., Ou et al., 2020). However, the peak time for the 9-km simulations is too late, which is even later than the IMERG observation (Figure 6a6). With further reduction in grid spacing below 10 km, the timing of diurnal precipitation peaks shifts earlier again, as shown in our results that WRF3 better captures the peak time compared to 9-km runs and improves the timing of precipitation peaks (Figure 6a7) and in studies that focused on other regions (e.g., Willetts et al., 2017; Yashiro et al., 2016). The later precipitation peaks in simulations with grid spacing around 10 km could be due to insufficient vertical moisture transport resolved by coarse model grids (Sato et al., 2009) and by not using the convection scheme at this grid scale, leading to later precipitation peaks than higher-resolution simulations. This pattern tends to occur over land; however, it is not consistent across all places (Ban et al., 2021). Although we have found the tendency to produce earlier precipitation in the WRF3, the time differences between WRF3 and WRF9 are often less than 3 hr and only over limited regions.

Figure 7 shows the mean diurnal cycle of the precipitation amount averaged over three latitude ranges (11°–13°, 16°–18°, and 20°–22°) from west to east of MSEA. The IMERG data set shows a higher precipitation rate over the three mountain ranges: Annamite Range (108°E in Figures 7b1 and 7c1), Tenasserim Hills (99°E in Figures 7b1 and 7c1), and Arakan Mountains (93°E in Figure 7a1) from 15 to 19 LST, as well as along the eastern and western coastlines of MSEA between 00 and 06 LST. ERA5 overestimates precipitation around 12–17 LST across most of MSEA, underestimates precipitation between late evening and morning, and does not capture the westward (eastward) propagation of precipitation from the eastern (western) coastline of MSEA after 14 LST. Conversely, the timing and westward/eastward propagation of precipitation in the WRF simulations aligned better with IMERG than ERA5. However, the WRF simulations overestimated precipitation over the three mountain ranges. These differences indicate the distinct spatiotemporal distribution of precipitation captured by the WRF and ERA5 models in the region. Based on the results presented in this section, the WRF3 does not exhibit a big

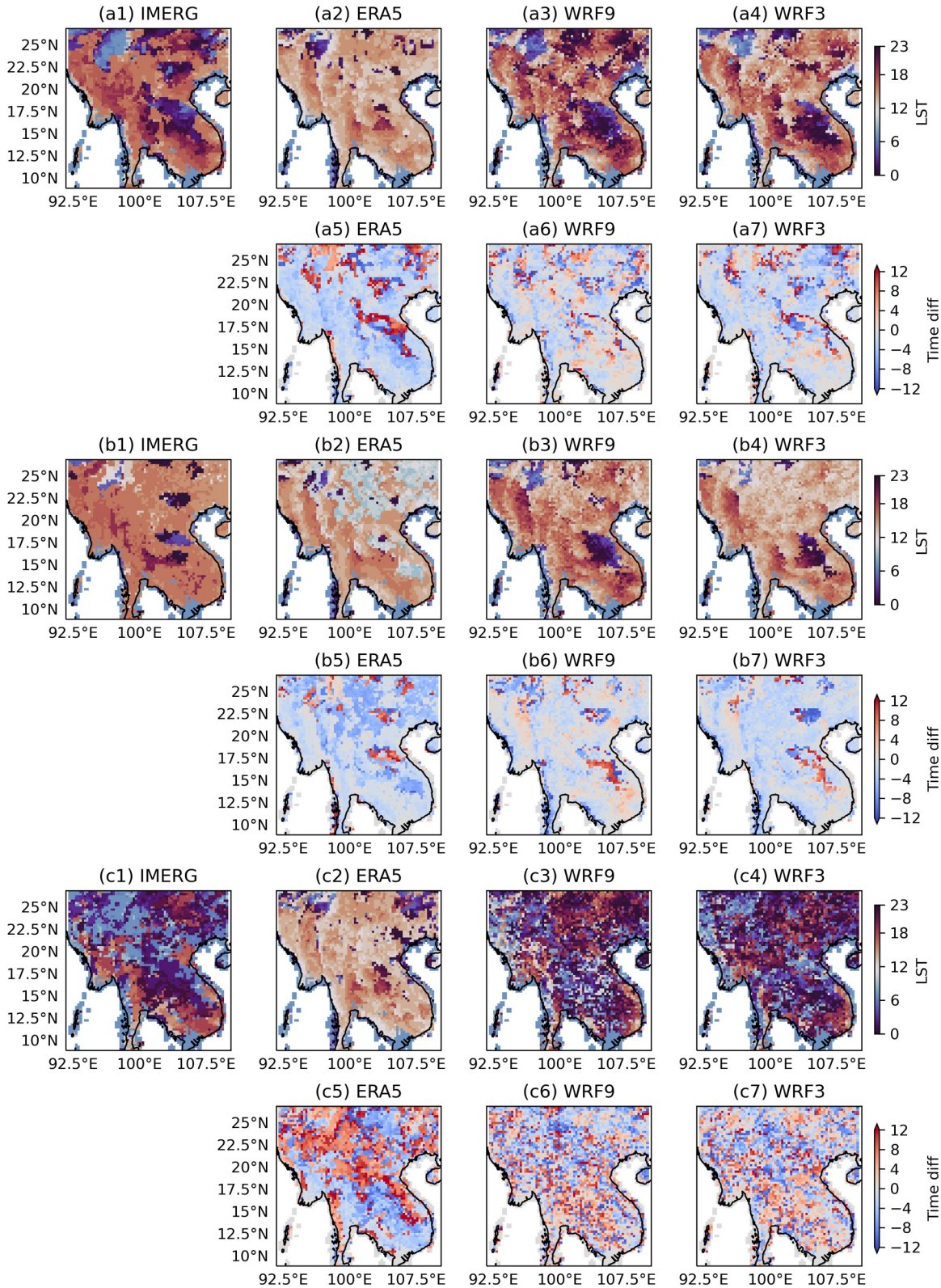

Figure 6. Spatial distributions of the diurnal peak time of hourly precipitation (a1–a7) amount, (b1–b7) frequency, and (c1–c7) intensity averaged over June-July-August of 2002–2005 for (a1–c1) Integrated Multi-Satellite Retrievals for Global Precipitation Measurement (IMERG), (a2, b2, and c2) ERA5, (a3, b3, and c3) WRF9, and (a4, b4, and c4) WRF3, and the difference in the peak time for (a5, b5, and c5) ERA5, (a6, b6, and c6) WRF9, and (a7, b7, and c7) WRF3 relative to IMERG.

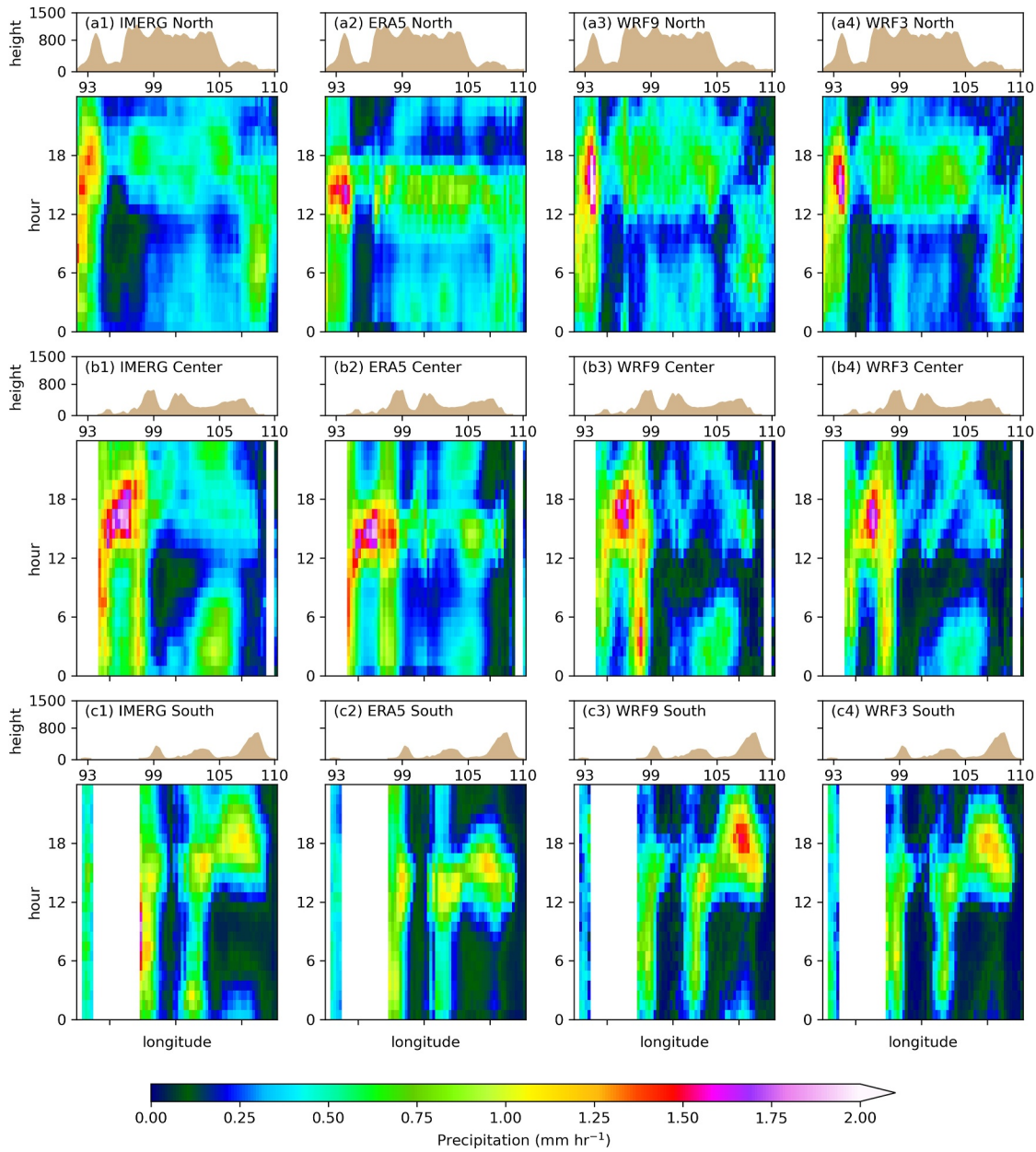

Figure 7. Hovmöller diagram of the diurnal precipitation variations averaged over June-July-August of 2002–2005 (color-shaded panels) over 91°–110°E averaged for three latitude zones: (a1–a4) northern (20°–22°N), (b1–b4) central (16°–18°N), and (c1–c4) southern (11°–13°N) parts of mainland Southeast Asia. The panels from left to right show the (a1, b1, and c1) IMERG, (a2, b2, and c2) ERA5, (a3, b3, and c3) WRF9, and (a4, b4, and c4) WRF3. The top small panels show the elevation of the terrain.

difference in simulating the peak time of the diurnal cycle of precipitation amount compared with WRF9. This raises the question of whether the CPM in the WRF3 simulation has added value in this case.

Overall, the spatial patterns of precipitation diurnal cycles are similar between WRF9 and WRF3. The main differences in precipitation between WRF9 and WRF3 simulations are mainly that WRF3 is drier and has an overall earlier precipitation peak than WRF9. In the next section, we will study how the two high-resolution WRF simulations capture the other atmospheric variables compared with ERA5, which could result in differences in the precipitation peak time and amount.

3.3. Possible Reasons for the Differences in the Diurnal Cycle of the Precipitation Between ERA5 and the Two WRF Simulations

We explored the possible physical mechanisms that account for the differences between the precipitation simulations shown in Figure 7 from ERA5 and WRF. The investigated variables include the CAPE, BLH, mean surface SHF, mean surface LHF, 10-m u-component of the wind (U10), 10-m v-component of the wind (V10), and atmospheric divergence at 10 m (DIV10). In the following sections, we divided the results into three subsections based on the key differences in modeling precipitation timing and magnitudes: (a) early precipitation peak in ERA5, (b) the evening and late-night precipitation regimes over mountainous areas, and (c) precipitation propagation close to the coastlines of MSEA.

3.3.1. Explanation of the Overall Diurnal Cycles of Precipitation in MSEA

Most areas in MSEA are classified in the two afternoon regimes (yellow and light red areas in Figures 5a–5d), which is associated with the maximum timing of CAPE (Figure 8). In addition, the early precipitation peaks across the entire domain in ERA5 could be associated with the fact that CAPE reached higher values earlier than in the WRF simulations (Figure 8). In ERA5, the timing of the precipitation peak is associated well with the first peak in the diurnal cycles of CAPE between 12 and 18 LST rather than the second peak after 18 LST (Figures 8a1, 8b1 and 8c1). This may be because most available perceptible water is released during the first peak. As precipitation begins, CAPE decreases due to moist convection consuming atmospheric energy (Dai, 2024). After precipitation ceases, CAPE rebuilds around 18 LST before gradually decreasing. The connection between the timing of precipitation peak and CAPE is stronger in central MSEA. In contrast, it is weaker in the mountain ranges (Figures 7a2, 7b2, 8a1, and 8b1) and along eastern coastlines (Figures 7b2 and 7c2), where the ERA5 failed to capture the early-morning precipitation and westward/eastward propagation of evening precipitation, respectively. In contrast, CAPE in WRF is lower than in ERA5 around 10–12 LST but continues to increase until 15 LST before precipitation initiates (Figures 8a2, 8a3, 8b2, and 8b3). Convective available potential energy is a physical measure of convective instability (Yano et al., 2013), in which the changes are the sum of changes induced by convective processes and by large-scale processes (G. J. Zhang, 2002). The convective processes are sensitive to model resolution, which may drive the difference in the peak times of CAPE in simulations with different resolutions. Agard and Emanuel (2017) also showed that temperature, surface moisture availability, and surface wind speed are all important determinants of the diurnal evolution of CAPE, which could be largely affected by evaporation. For example, the ERA5 tends to have larger evaporation than WRF simulation (X. Liu et al., 2025), which may lead to an earlier peak of CAPE due to higher moisture availability. In this study, the difference in timing of high CAPE suggests that convection is triggered later in WRF compared to ERA5, likely due to model resolution and its impact on key thermodynamic variables as well as the trigger function.

The WRF simulations generally produce stronger CAPE than ERA5 across both low and high elevations (Figure 8), likely due to differences in atmospheric stability. Our analysis of vertical cross-sections of equivalent potential temperature (θ_e) in several subregions—Khorat Plateau (16°–18°N), southern MSEA (11°–13°N), the western coast (12°–17°N), and over the northern mountain range (24°–26°N)—shows key differences between ERA5 and WRF (Figure S3 in Supporting Information S1). Specifically, WRF simulates a warmer θ_e in the middle troposphere (600 hPa over the northern mountains and 700–800 hPa over southern MSEA and the Khorat Plateau) in WRF, as well as a warmer near-surface layer over the ocean along the western coastline. The warmer middle atmosphere in WRF reduces stability between the surface and mid-atmosphere, an effect more pronounced during the daytime across all regions. This reduced stability likely contributes to the higher CAPE in WRF than ERA5 over the Khorat Plateau and western coastlines. However, this relationship does not hold over the northern mountains and southern MSEA, where nighttime CAPE in WRF is lower than in ERA5.

However, unlike CAPE, WRF precipitation is not consistently higher than that of ERA5 (Figures 8a2, 8b2, 8c2, 8a3, 8b3, 8c3, 8a4, 8b4, and 8c4), suggesting that additional factors could play an important role in driving the diurnal precipitation in the WRF model. In the WRF simulations, the precipitation intensity can be higher during the late night and morning along the coastlines when CAPE is usually low. Therefore, the link between CAPE and precipitation is weaker in the WRF simulations than in ERA5. Studies have shown that the absence of a cumulus scheme in the high-resolution simulations could result in a more accurate simulation of the peak precipitation times (P. Li et al., 2021; Z. Liu et al., 2022). In contrast, ERA5 simulations tend to produce early afternoon precipitation, likely due to early peaks in diurnal CAPE. This aligns with previous findings that weather and

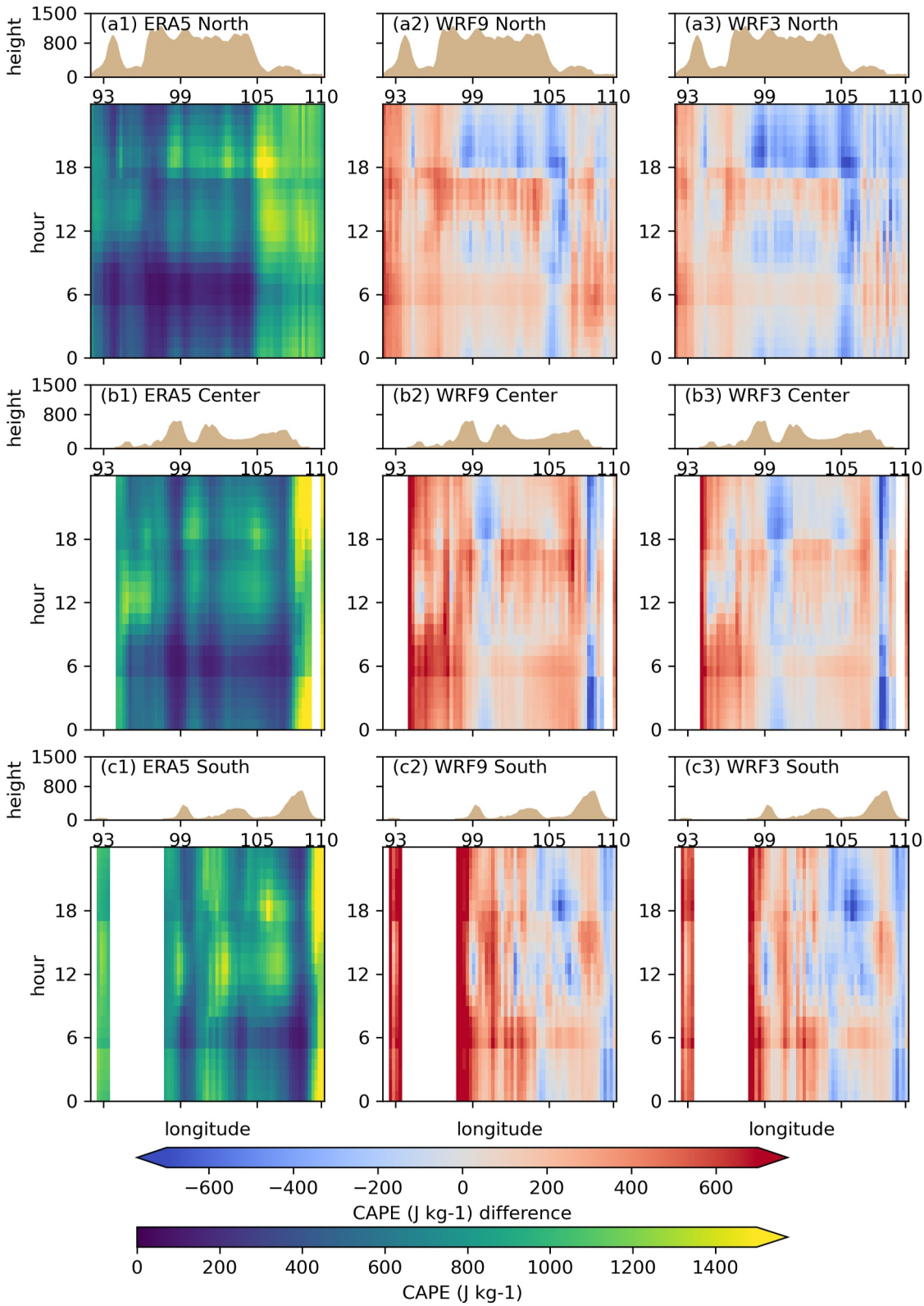

Figure 8. Hovmöller diagram of the convective available potential energy over 91°–110°E averaged for three latitude ranges: (a1–a3) northern (20°–22°N), (b1–b3) central (16°–18°N), and (c1–c3) southern (11°–13°N) parts of mainland Southeast Asia averaged over June-July-August of 2002–2005. The panels from left to right are the (a1, b1, and c1) ERA5, (a2, b2, and c2) WRF9 minus ERA5, (a3, b3, and c3) WRF3 minus ERA5. The top small panels show the elevation of the terrain.

climate models often trigger rainfall too early over land, suggesting that refining the CAPE trigger function could help improve this issue (Xie et al., 2019). Our results further confirm that employing high-resolution modeling is essential for better capturing diurnal cycles of precipitation in MSEA.

Between the two WRF simulations, CAPE from WRF3 is less than that in WRF9 for the three study regions (Figures 8a2–8c3). This could be one of the reasons that WRF3 precipitation is less than WRF9 (Figures 7a3–7c4). However, the magnitude differences in CAPE between WRF9 and WRF3 are systematic across the regions and time. Therefore, we further explore other variables that could cause the variations in spatiotemporal patterns of the WRF precipitation.

3.3.2. Explanation of the Evening–Morning Regimes Over Mountainous Areas

The ERA5 does not capture the evening and late-night regimes to the east of the Khorat Plateau and northern MSEA, while the classifications with IMERG and the WRF simulations show these regimes (Figures 5a–5d). Figures 7a2, 7b2, and 7c2 show that ERA5 does produce the evening and late-night precipitation around 105°E. However, ERA5 produces peaks of precipitation amount in the afternoon while the other data sets show the evening and late-night precipitation only. The afternoon peak in ERA5 could be associated with the timing of CAPE peaks (Figures 8a1, 8b1, and 8c1).

The precipitation peaks from WRF simulations do not completely match the timing of CAPE peaks in the afternoon. Although the two WRF simulations also produce peaks of CAPE in the afternoon, the evening and late-night precipitation is associated with higher CAPE rather than the peaks in the afternoon (Figures 8a2–8c3). In addition, the morning peaks of precipitation amount in the east of the Khorat Plateau, and late-night–morning precipitation peaks are found to be associated with local convergence (shading in Figure 9). The connections between late-night to morning precipitation and low-level convergence can be seen especially over the mountainous areas. The identified processes agree with previous findings that the early-morning peak could be caused by nighttime radiative cooling, which enhances low-level convergence and causes the early-morning development of convective systems (Lu et al., 2021). Both ERA5 and WRF simulations capture the evening and late-night precipitation. However, WRF simulates these periods with higher intensities than the afternoon precipitation, allowing k-means to classify several regions as evening and late-night regimes. On the other hand, the absence of evening and late-night regimes in ERA5 is not due to its inability to produce precipitation during those periods, but rather the result of the excessive afternoon precipitation related to the CAPE peaks.

3.3.3. Precipitation Propagation Close to the Coastlines

The IMERG data show clear westward (eastward) propagation of precipitation bands in the afternoon along the eastern (western) coastlines (Figures 7a1–7c1), a feature that ERA5 barely captured, while the WRF simulation successfully reproduced it (Figure 7a2–7c4). By examining U10 anomalies (relative to the daily mean), we identified sea breeze signals along the coastlines in both ERA5 and WRF simulations. The sea breeze signals could be identified with anomalous onshore winds (contours in Figure 9) and low-level convergence (shading in Figure 9) along the coastlines (Peng & Chen, 2024). ERA5 shows generally weaker onshore winds at key longitudes (108°E in the central and south regions, 100°E in the south, 95°E in the central region, and 93°E in the north) than the two WRF simulations, and ERA5 does not capture the onshore propagation of the convergence anomalies after 12 LST. In contrast, the WRF simulation produced strong onshore winds and the westward (eastward) propagation of convergence anomalies from the eastern (western) coastlines (Figure 9). This comparison highlights WRF's ability to capture the timing of precipitation peaks, particularly from evening to morning, due to its representation of sea breeze circulation. ERA5 does not capture surface diurnal winds over ocean and coastal areas because it uses daily mean SST as the lower boundary (Dai, 2023). This limitation could impact ERA5's ability to accurately simulate the diurnal sea breeze. A recent study found that GCMs struggle to properly simulate diurnal precipitation over land and coastal land, and suggested that improvements in convection triggering and topography representation in the models could be key to addressing this issue (Tao et al., 2023). Our results confirm that high-resolution WRF modeling could better simulate U10 and convergence, which are essential processes triggering the diurnal precipitation along coastlines over MSEA.

The U10 and convergence anomalies from the two WRF simulations share a similar spatial distribution, although WRF3 exhibits a weaker U10 intensity. Compared to WRF9, WRF3 simulated generally weaker large-scale winds but exhibited stronger divergence and convergence near mountains and coastlines, which may have

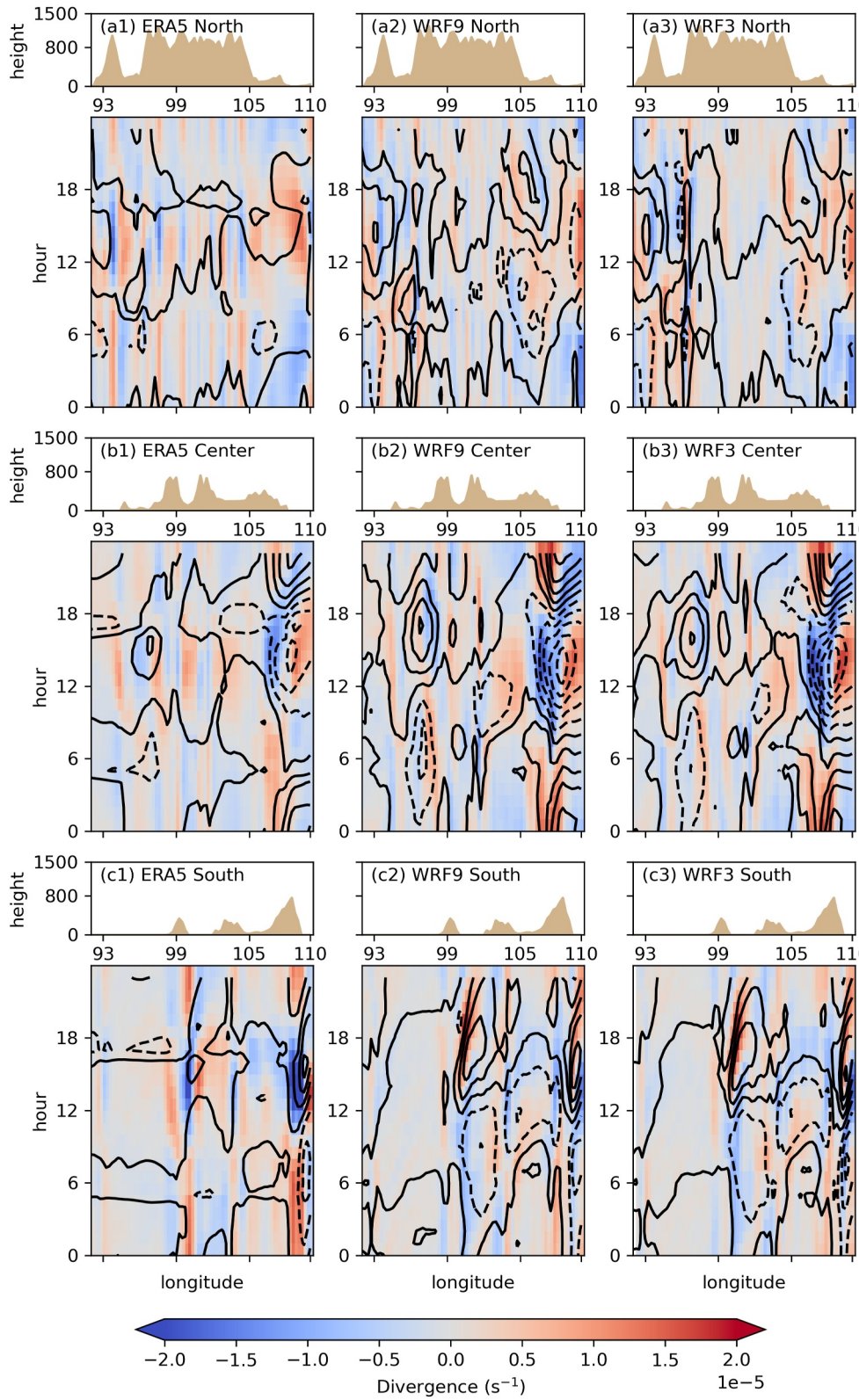

Figure 9. Hovmöller diagram of the u10 (10-m zonal wind, contours) and 10-m divergence (shading) anomalies (relative to the daily mean) over 91°–110°E averaged for three latitude ranges: (a1–a3) northern (22°–24°N), (b1–b3) central (16°–18°N), and (c1–c3) southern (11°–13°N) parts of mainland Southeast Asia averaged over June-July-August of 2002–2005. The panels from left to right are the (a1, b1, and c1) ERA5, (a2, b2, and c2) WRF9, and (a3, b3, and c3) WRF3. The positive (negative) u10 is shown as solid (dashed) contours with 0.5-m s^{-1} intervals. The top small panels show the elevation of the terrain.

contributed to the overall weaker precipitation with local intensive precipitation in the WRF3 simulations. In our study, the WRF3 simulations captured the overall diurnal precipitation well, while WRF9 tended to overestimate precipitation, mostly during the main precipitation periods.

Overall, the differences in the processes simulated by ERA5 and WRF models are reflected in CAPE and near-surface winds in terms of their diurnal timing, magnitude, and spatial distribution. The atmospheric variables from the two WRF simulations share a similar spatial distribution while in the WRF3, the variables such as the U10 and CAPE exhibit weaker diurnal anomalies, except for surface SHF (not shown). The weaker U10 and CAPE in WRF3 could lead to lower precipitation amount and intensity than WRF9 (Figures 4a and 4c).

To ensure the sea breeze patterns simulated by WRF are reasonable, we evaluated the near-surface winds in the models using wind analysis from CCMP. The 6-hourly CCMP wind anomalies at 10 m (relative to the daily mean) show offshore and onshore winds along the eastern coastline around 00 and 12 UTC (Figures 10a1, 10a3), indicating a sea/land breeze circulation. ERA5 overestimates the north-south wind components over both land and ocean while showing weaker onshore/offshore components along the coastlines in the diurnal cycles (Figures 10b1–10b4). On the other hand, the two WRF simulations capture offshore and onshore winds at the eastern coastline at 00 and 12 UTC (Figures 10d1 and 10d3), which has been shown in the previous findings (Figures 9a2, 9b2, 9c2, 9a3, 9b3, and 9c3) and remain consistent with CCMP. Previous studies have highlighted that simulated wind directions, speeds, and precipitation over complex topography are highly dependent on model resolution (e.g., Johnson et al., 2016; Wu et al., 2017), suggesting that high-resolution modeling may more effectively capture the timing and magnitudes of diurnal winds (e.g., Belušić et al., 2018; Gil Ruiz et al., 2022). In this study, we do not see large differences in diurnal winds between WRF9 and WRF3. Further evaluation of high-resolution local winds is needed to explore the benefits of RCM and CPM simulations. Nevertheless, to better simulate the diurnal precipitation, the results highlight the importance of applying high-resolution models to simulate near-surface winds.

4. Uncertainties and Challenges

The added value of high-resolution modeling could differ for different variables and regions. Previous studies have suggested that CPMs could have benefits related to moisture transport (Zhao et al., 2021), convection propagation (Rasmussen et al., 2020), and events that occur over complex terrain (Belušić Vozila et al., 2023). In our study, the CPM (WRF3) was found to more effectively capture the heavy daily precipitation, but it had less added value in terms of simulating the average diurnal cycle of the precipitation than the RCM (WRF9). For example, WRF3 and WRF9 perform similarly in diurnal precipitation locations, peak timing, and bias. Recent studies suggest that resolutions below 10 km may offer limited improvement in precipitation simulation. For example, Taraphdar et al. (2021) found that the 'gray-zone' resolution (9 km) performs comparably to 5 km, while other studies indicate that 1–3 km may be sufficient for capturing precipitation (Ito et al., 2017; Jeworrek et al., 2019). Our results provide insights into how high-resolution modeling captures diurnal precipitation characteristics, which is essential for improving future climate projections, particularly in regions with complex topography and strong diurnal cycles. Understanding the biases and uncertainties in different model resolutions can help refine convection schemes and microphysics parameterizations in future climate simulations. These improvements are critical for assessing changes in extreme precipitation and hydrological impacts under future climate scenarios.

Another challenge in evaluating the added value of CPMs such as WRF3 is the limited availability of high-resolution observations. This lack of high-resolution observations, especially gridded observations, could result in a poor understanding of the physical processes related to the local precipitation (Kendon et al., 2021; Lucas-Picher et al., 2021). In our study, the precipitation simulations of the western coast of MSEA, the eastern Khorat Plateau, and the northern mountainous areas were improved, but limited in situ observations were available in these regions. While we attempted to address the processes by using the ERA5 data as a reference, further intensive local observations are needed to strengthen the findings.

The choice of physical parameterization schemes in WRF introduces inherent uncertainties in the simulation results. Different schemes for microphysics, planetary boundary layer, and radiation processes influence cloud formation, precipitation intensity, and energy fluxes, leading to variations in model performance. Related studies focusing on our WRF9 domain have shown that the main sources of uncertainties come from microphysics and planetary boundary layer schemes (Prein et al., 2023), though most kilometer-scale simulations with various parameterizations improve the early onset and peak timing of diurnal precipitation (Collier et al., 2024). While

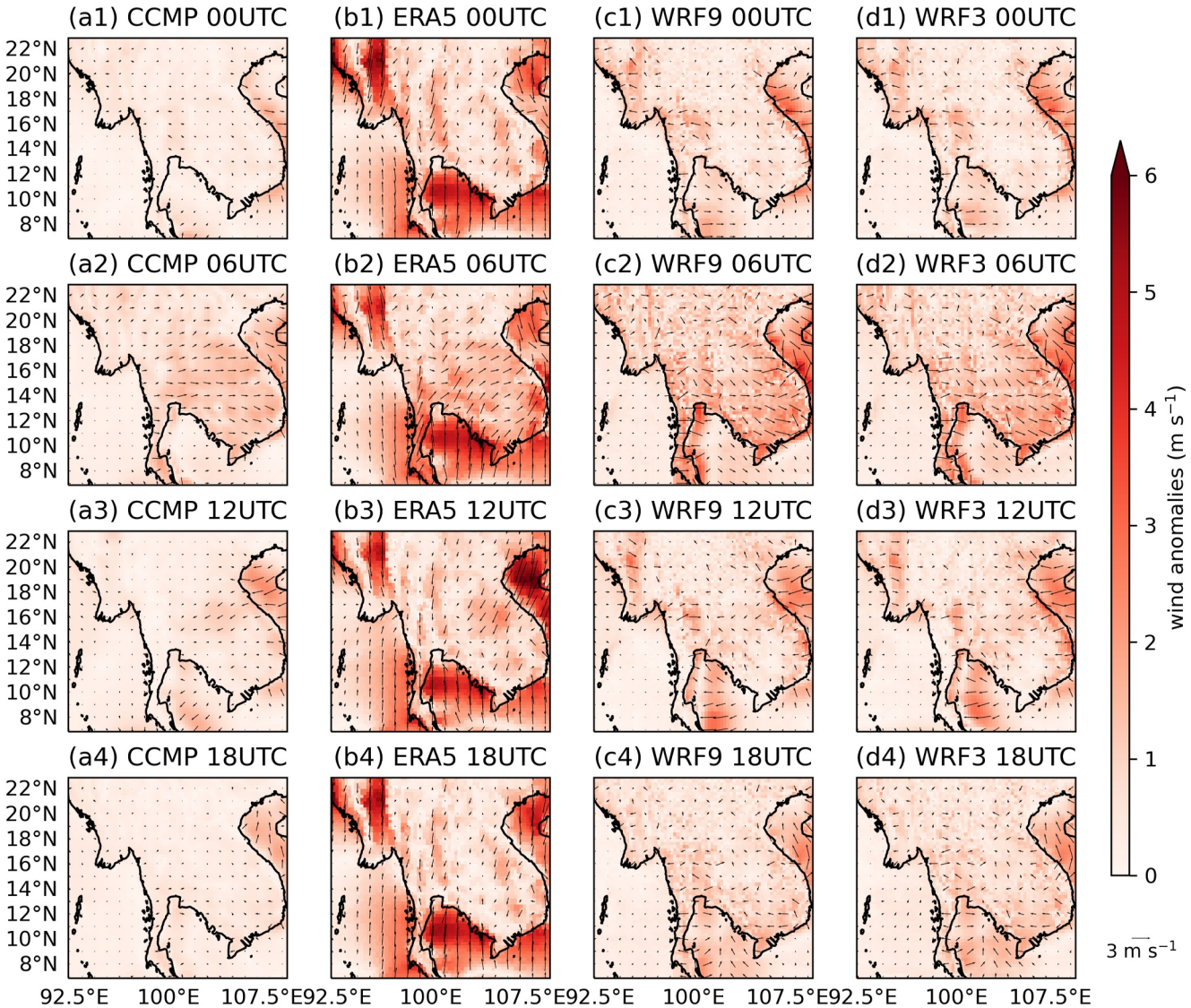

Figure 10. Spatial distribution of 10-m wind anomalies (relative to the daily mean) for (a) cross-calibrated multiplatform project, (b) ERA5, (c) WRF9, and (d) WRF3 averaged over June-July-August of 2002–2005. The panels from top to bottom are the wind anomalies at (1) 00, (2) 06, (3) 12, and (4) 18 UTC.

our model setup follows best practices from previous studies, a comprehensive sensitivity analysis is needed to fully assess the impact of different schemes on diurnal precipitation simulation.

Lastly, we recognize the uncertainties in observation-based data sets. Our evaluation used multiple data sets, including station-based data from GHCN-D and Wang et al. (2016) as well as APHRODITE, MSWEP, and IMERG. APHRODITE, based solely on rain gauge data, is limited by station density and may not fully capture extremes. The station-based data sets were considered the reference in this study. However, their daily resolution limits the assessment of diurnal precipitation. We explored subdaily data from HadISD and inquired about other data sets, but the available records were insufficient for this study. There is a clear need for more comprehensive subdaily precipitation data sets, particularly in this region. IMERG has been reported to show higher uncertainties when a large proportion of precipitation falls as snow (Z. Li et al., 2023), while MSWEP has greater uncertainties before 2000 due to limited constraints from surface observations (Beck et al., 2019). However, these issues have limited impact on our study, which focuses on summertime diurnal precipitation after 2000. MSWEP and IMERG help bridge spatial and temporal gaps. IMERG is available on an hourly scale, while MSWEP is only available on a 3-hr scale. In the analysis of the diurnal cycle, we mainly based on IMERG. However, they also have known biases—IMERG exhibits a phase lag in precipitation amount (Dai, 2024), while MSWEP tends to produce earlier

precipitation peaks and underestimates diurnal amplitude (Dong et al., 2023). The combination of MSWEP and IMERG could give a reasonable range of the observations. Figure 4 agrees with the previous work regarding the peak time for IMERG and MSWEP. IMERG and MSWEP have a similar diurnal cycle, except for IMERG with a later peak time. There may be a 1–3-hr uncertainty in the peak time calculated by hourly IMERG. Given the later peak in IMERG as reported by previous work, the model simulation may give better results providing more precise hourly precipitation estimates. These data set-specific uncertainties impact model evaluation, particularly in capturing precipitation timing, intensity, and frequency, and should be carefully considered in future studies.

5. Conclusions

In this study, we investigated the diurnal cycles of summer precipitation and related atmospheric variables over MSEA using surface and satellite observations, ERA5, and high-resolution WRF simulations. Specifically, we downscaled the ERA5 data to finer resolutions of 3- and 9-km grid spacing using the WRF model and explored the characteristics of precipitation patterns and the benefits of employing high-resolution models.

The key findings of this study are as follows.

1. Compared with MSWEP 3-hourly precipitation, ERA5 overestimates precipitation amount and frequency. On the other hand, IMERG produces a later peak of precipitation amount, and lower precipitation frequency than MSWEP. The two WRF simulations have similar results to IMERG and the precipitation histograms from WRF3 are closer to IMERG than WRF9.
2. k-means classification of the IMERG precipitation data identified five spatial regimes with distinct diurnal cycles, characterized by specific precipitation peaks at different times of a day. These regimes include precipitation peaks at late night, morning, afternoon (two peaks), and evening. It provides a comprehensive insight into the spatial distribution of the precipitation diurnal cycle across MSEA.
3. ERA5 consistently shows earlier diurnal precipitation peaks (2–5 hr earlier) across MSEA than IMERG due to early CAPE peaks. In addition, ERA5 does not capture late-night to morning peaks in mountainous areas and morning peaks along western coastlines because of excessive CAPE peaks, which mask evening and late-night regimes.
4. Both WRF simulations capture the distinct diurnal peaks of precipitation amount, frequency, and intensity closer to IMERG than ERA5. The WRF simulations also closely reproduce the spatial patterns of precipitation regimes seen in IMERG, especially for late-night to morning precipitation peaks in mountainous regions, eastward propagation of precipitation on the eastern coastlines, and morning peaks on the western coastline. Differences in precipitation timing and amount between ERA5 and WRF are linked to spatiotemporal variations in CAPE and near-surface wind simulations.
5. WRF3 produces less precipitation with an earlier peak due to weaker large-scale winds and stronger local convergence near mountains and coastlines than WRF9. It captures the distribution of heavy precipitation and the diurnal cycles of frequency and intensity seen in IMERG better than WRF9. WRF9 tends to overestimate precipitation during peak periods.
6. High-resolution WRF simulations are crucial for accurately capturing diurnal precipitation cycles. While WRF3 shows weaker U10 and CAPE than WRF9, it better represents specific precipitation characteristics seen in IMERG. The benefits of high-resolution modeling vary by regions and variables, highlighting the need for further high-resolution observations and assessments to fully understand its advantages.

Data Availability Statement

The ERA5 data were obtained from the Copernicus Climate Data Store (Hersbach et al., 2020). The GPM IMERG data were downloaded from the GES DISC (G. J. Huffman et al., 2019) and the MSWEP data were from GloH2O (Beck et al., 2019). The GHCN-D data are available from the National Centers for Environmental Information (Menne et al., 2012). The precipitation data from APHRODITE were obtained from the APHRODITE's Water Resources Project (Yatagai et al., 2012). The near-surface winds from CCMP can be found at PO.DAAC (Mears et al., 2022). The WRF simulations can be downloaded from the Regional Climate Group's website (Ou et al., 2023).

Acknowledgments
This work was supported by the Strategic Priority Research Program of the Chinese Academy of Sciences (XDA20060401) and the Swedish Foundation for International Cooperation in Research and Higher Education (CH2019-8377 and CH2020-8767). We thank Prof. Deliang Chen for the insightful discussions that contributed to this study. This is a contribution to the Swedish national strategic research program MERGE. The computations/data handling were enabled by resources provided by the National Academic Infrastructure for Supercomputing in Sweden (NAISS). A.D. was supported by NSF award no. AGS-2015780.

References

Agard, V., & Emanuel, K. (2017). Clausius–Clapeyron scaling of peak CAPE in continental convective storm environments. *Journal of the Atmospheric Sciences*, *74*(9), 3043–3054. https://doi.org/10.1175/JAS-D-16-0352.1

Ban, N., Caillaud, C., Coppola, E., Pichelli, E., Sobolowski, S., Adinolfi, M., et al. (2021). The first multi-model ensemble of regional climate simulations at kilometer-scale resolution, part I: Evaluation of precipitation. *Climate Dynamics*, *57*(1–2), 275–302. https://doi.org/10.1007/s00382-021-05708-w

Beck, H. E., Wood, E. F., Pan, M., Fisher, C. K., Miralles, D. G., van Dijk, A. I. J. M., et al. (2019). MSWEP V2 global 3-hourly 0.1° precipitation: Methodology and quantitative assessment [Dataset]. *Bulletin of the American Meteorological Society*, *100*(3), 473–500. https://doi.org/10.1175/BAMS-D-17-0138.1

Belušić, A., Prtenjak, M. T., Güttler, I., Ban, N., Leutwyler, D., & Schär, C. (2018). Near-surface wind variability over the broader adriatic region: Insights from an ensemble of regional climate models. *Climate Dynamics*, *50*(11–12), 4455–4480. https://doi.org/10.1007/s00382-017-3885-5

Belušić Vozila, A., Belušić, D., Telišman Prtenjak, M., Güttler, I., Bastin, S., Brisson, E., et al. (2023). Evaluation of the near-surface wind field over the Adriatic region: Local wind characteristics in the convection-permitting model ensemble. *Climate Dynamics*, *62*(6), 4617–4634. https://doi.org/10.1007/s00382-023-06703-z

Biasutti, M., Yuter, S. E., Burleyson, C. D., & Sobel, A. H. (2012). Very high resolution rainfall patterns measured by TRMM precipitation radar: Seasonal and diurnal cycles. *Climate Dynamics*, *39*(1–2), 239–258. https://doi.org/10.1007/s00382-011-1146-6

Chakraborty, T., Pattnaik, S., Jenamani, R. K., & Baisya, H. (2021). Evaluating the performances of cloud microphysical parameterizations in WRF for the heavy rainfall event of Kerala (2018). *Meteorology and Atmospheric Physics*, *133*(3), 707–737. https://doi.org/10.1007/s00703-021-00776-3

Chan, M., Chen, X., & Leung, L. R. (2022). A high-resolution tropical mesoscale convective system reanalysis (TMeCSR). *Journal of Advances in Modeling Earth Systems*, *14*(9). https://doi.org/10.1029/2021MS002948

Chen, D., & Dai, A. (2018). Dependence of estimated precipitation frequency and intensity on data resolution. *Climate Dynamics*, *50*(9–10), 3625–3647. https://doi.org/10.1007/s00382-017-3830-7

Chen, D., & Dai, A. (2019). Precipitation characteristics in the community atmosphere model and their dependence on model physics and resolution. *Journal of Advances in Modeling Earth Systems*, *11*(7), 2352–2374. https://doi.org/10.1029/2018MS001536

Chen, D., Dai, A., & Hall, A. (2021). The convective-to-total precipitation ratio and the "drizzling" bias in climate models. *Journal of Geophysical Research: Atmospheres*, *126*(16), e2020JD034198. https://doi.org/10.1029/2020JD034198

Chen, P., Chen, A., Yin, S., Li, Y., & Liu, J. (2024). Clustering the diurnal cycle of precipitation using global satellite data. *Geophysical Research Letters*, *51*(23), e2024GL111513. https://doi.org/10.1029/2024GL111513

Chen, X., Pauluis, O. M., & Zhang, F. (2018). Regional simulation of Indian summer monsoon intraseasonal oscillations at gray-zone resolution. *Atmospheric Chemistry and Physics*, *18*(2), 1003–1022. https://doi.org/10.5194/acp-18-1003-2018

Chung, J. X., Juneng, L., Santisirisomboon, G., Ngo-Duc, T., Phan-Van, T., Trinh-Tuan, L., et al. (2023). Future changes in mean and extreme precipitation over Peninsular Malaysia using CORDEX-SEA 5 km simulations. *APN Science Bulletin*, *13*(1), 263–276. https://doi.org/10.30852/sb.2023.2348

Collier, E., Ban, N., Richter, N., Ahrens, B., Chen, D., Chen, X., et al. (2024). The first ensemble of kilometer-scale simulations of a hydrological year over the third pole. *Climate Dynamics*, *62*(8), 7501–7518. https://doi.org/10.1007/s00382-024-07291-2

Curio, J., & Scherer, D. (2016). Seasonality and spatial variability of dynamic precipitation controls on the Tibetan Plateau. *Earth System Dynamics*, *7*(3), 767–782. https://doi.org/10.5194/esd-7-767-2016

Dai, A. (2023). The diurnal cycle from observations and ERA5 in surface pressure, temperature, humidity, and winds. *Climate Dynamics*, *61*(5–6), 2965–2990. https://doi.org/10.1007/s00382-023-06721-x

Dai, A. (2024). The diurnal cycle from observations and ERA5 in precipitation, clouds, boundary layer height, buoyancy, and surface fluxes. *Climate Dynamics*. https://doi.org/10.1007/s00382-024-07182-6

Dai, A., Lin, X., & Hsu, K.-L. (2007). The frequency, intensity, and diurnal cycle of precipitation in surface and satellite observations over low- and mid-latitudes. *Climate Dynamics*, *29*(7–8), 727–744. https://doi.org/10.1007/s00382-007-0260-y

Dangol, S., Talchabhadel, R., & Pandey, V. P. (2022). Performance evaluation and bias correction of gridded precipitation products over Arun River Basin in Nepal for hydrological applications. *Theoretical and Applied Climatology*, *148*(3–4), 1353–1372. https://doi.org/10.1007/s00704-022-04001-y

Dirmeyer, P. A., Cash, B. A., Kinter, J. L., Jung, T., Marx, L., Satoh, M., et al. (2012). Simulating the diurnal cycle of rainfall in global climate models: Resolution versus parameterization. *Climate Dynamics*, *39*(1–2), 399–418. https://doi.org/10.1007/s00382-011-1127-9

Dong, W., Krasting, J. P., & Guo, H. (2023). Analysis of precipitation diurnal cycle and variance in multiple observations, CMIP6 models, and a series of GFDL-AM4.0 simulations. *Journal of Climate*, *36*(24), 8637–8655. https://doi.org/10.1175/JCLI-D-23-0268.1

ECMWF. (n.d.). Parameter detail. Retrieved from https://codes.ecmwf.int/grib/param-db/228

Elahi, E., Abro, M. I., Khaskheli, M. A., Kandhro, G. A., Zehra, T., Ali, S., et al. (2024). Long-term evaluation of rainfall in the arid region of Pakistan using multi-source data. *Theoretical and Applied Climatology*, *155*(4), 2819–2840. https://doi.org/10.1007/s00704-023-04797-3

Ferrett, S., Frame, T. H. A., Methven, J., Holloway, C. E., Webster, S., Stein, T. H. M., & Cafaro, C. (2021). Evaluating convection-permitting ensemble forecasts of precipitation over Southeast Asia. *Weather and Forecasting*, *36*(4), 1199–1217. https://doi.org/10.1175/WAF-D-20-0216.1

Gil Ruiz, S. A., Cañón Barriga, J. E., & Martínez, J. A. (2022). Assessment and validation of wind power potential at convection-permitting resolution for the Caribbean region of Colombia. *Energy*, *244*, 123127. https://doi.org/10.1016/j.energy.2022.123127

Gupta, A., Jain, M. K., Pandey, R. P., Gupta, V., & Saha, A. (2024). Evaluation of global precipitation products for meteorological drought assessment with respect to IMD station datasets over India. *Atmospheric Research*, *297*, 107104. https://doi.org/10.1016/j.atmosres.2023.107104

Hariadi, M. H., van der Schrier, G., Steeneveld, G., Ratri, D. N., Sopaheluwakan, A., Tank, A. K., et al. (2023). Evaluation of extreme precipitation over Southeast Asia in the coupled model intercomparison project phase 5 regional climate model results and HighResMIP global climate models. *International Journal of Climatology*, *43*(3), 1639–1659. https://doi.org/10.1002/joc.7938

Hayden, L., & Liu, C. (2021). Differences in the diurnal variation of precipitation estimated by spaceborne radar, passive microwave radiometer, and IMERG. *Journal of Geophysical Research: Atmospheres*, *126*(9), e2020JD033020. https://doi.org/10.1029/2020JD033020

Hayden, L. J. M., Tan, J., Bolvin, D. T., & Huffman, G. J. (2023). Variations in the diurnal cycle of precipitation and its changes with distance from shore over two contrasting regions as observed by IMERG, ERA5, and spaceborne Ku radar. *Journal of Hydrometeorology*, *24*(4), 675–689. https://doi.org/10.1175/JHM-D-22-0154.1

Hersbach, H., Bell, B., Berrisford, P., Hirahara, S., Horányi, A., Muñoz-Sabater, J., et al. (2020). The ERA5 global reanalysis [Dataset]. *Quarterly Journal of the Royal Meteorological Society*, *146*(730), 1999–2049. https://doi.org/10.1002/qj.3803

Hong, S.-Y., Noh, Y., & Dudhia, J. (2006). A new vertical diffusion package with an explicit treatment of entrainment processes. *Monthly Weather Review*, *134*(9), 2318–2341. https://doi.org/10.1175/MWR3199.1

Huffman, G. J., Bolvin, D. T., Braithwaite, D., Hsu, K.-L., Joyce, R. J., Kidd, C., et al. (2020). Integrated multi-satellite retrievals for the global precipitation measurement (GPM) mission. *IMERG*, 343–353. https://doi.org/10.1007/978-3-030-24568-9_19

Huffman, G. J., Stocker, E. F., Bolvin, D. T., Nelkin, E. J., & Tan, J. (2019). [Dataset], *GPM IMERG final precipitation L3 1 day 0.1 degree x 0.1 degree V06*. In A. Savtchenko (Ed.). Goddard Earth Sciences Data and Information Services Center (GES DISC). https://doi.org/10.5067/GPM/IMERGDF/DAY/06

Iacono, M. J., Delamere, J. S., Mlawer, E. J., Shephard, M. W., Clough, S. A., & Collins, W. D. (2008). Radiative forcing by long-lived greenhouse gases: Calculations with the AER radiative transfer models. *Journal of Geophysical Research*, *113*(D13), D13103. https://doi.org/10.1029/2008JD009944

Ito, J., Hayashi, S., Hashimoto, A., Ohtake, H., Uno, F., Yoshimura, H., et al. (2017). Stalled improvement in a numerical weather prediction model as horizontal resolution increases to the sub-kilometer scale. *SOLA*, *13*, 151–156. https://doi.org/10.2151/sola.2017-028

Jeworrek, J., West, G., & Stull, R. (2019). Evaluation of cumulus and microphysics parameterizations in WRF across the convective gray zone. *Weather and Forecasting*, *34*(4), 1097–1115. https://doi.org/10.1175/WAF-D-18-0178.1

Johnson, S. J., Levine, R. C., Turner, A. G., Martin, G. M., Woolnough, S. J., Schiemann, R., et al. (2016). The resolution sensitivity of the South Asian monsoon and Indo-Pacific in a global 0.35° AGCM. *Climate Dynamics*, *46*(3–4), 807–831. https://doi.org/10.1007/s00382-015-2614-1

Jones, R. W., Sanchez, C., Lewis, H., Warner, J., Webster, S., & Macholl, J. (2023). Impact of domain size on tropical precipitation within explicit convection simulations. *Geophysical Research Letters*, *50*(17), e2023GL104672. https://doi.org/10.1029/2023GL104672

Kendon, E. J., Prein, A. F., Senior, C. A., & Stirling, A. (2021). Challenges and outlook for convection-permitting climate modelling. *Philosophical Transactions of the Royal Society A: Mathematical, Physical and Engineering Sciences*, *379*(2195), 20190547. https://doi.org/10.1098/rsta.2019.0547

Van Khiem, M., Redmond, G., McSweeney, C., & Thuc, T. (2014). Evaluation of dynamically downscaled ensemble climate simulations for Vietnam. *International Journal of Climatology*, *34*(7), 2450–2463. https://doi.org/10.1002/joc.3851

Kim, H., Lee, M.-I., Cha, D.-H., Lim, Y.-K., & Putman, W. M. (2019). Improved representation of the diurnal variation of warm season precipitation by an atmospheric general circulation model at a 10 km horizontal resolution. *Climate Dynamics*, *53*(11), 6523–6542. https://doi.org/10.1007/s00382-019-04943-6

Kuenzer, C., & Knauer, K. (2013). Remote sensing of rice crop areas. *International Journal of Remote Sensing*, *34*(6), 2101–2139. https://doi.org/10.1080/01431161.2012.738946

Li, P., Furtado, K., Zhou, T., Chen, H., & Li, J. (2021). Convection-permitting modelling improves simulated precipitation over the central and eastern Tibetan Plateau. *Quarterly Journal of the Royal Meteorological Society*, *147*(734), 341–362. https://doi.org/10.1002/qj.3921

Li, R., Wang, K., & Qi, D. (2018). Validating the integrated multisatellite retrievals for global precipitation measurement in terms of diurnal variability with hourly gauge observations collected at 50,000 stations in China. *Journal of Geophysical Research: Atmospheres*, *123*(18), 10423–10442. https://doi.org/10.1029/2018JD028991

Li, Z., Wright, D. B., Hartke, S. H., Kirschbaum, D. B., Khan, S., Maggioni, V., & Kirstetter, P.-E. (2023). Toward a globally-applicable uncertainty quantification framework for satellite multisensor precipitation products based on GPM DPR. *IEEE Transactions on Geoscience and Remote Sensing*, *61*, 1–15. https://doi.org/10.1109/TGRS.2023.3235270

Liang, X., Li, L., Dai, A., & Kunkel, K. E. (2004). Regional climate model simulation of summer precipitation diurnal cycle over the United States. *Geophysical Research Letters*, *31*(24), L24208. https://doi.org/10.1029/2004GL021054

Lim, K.-S. S., & Hong, S.-Y. (2010). Development of an effective double-moment cloud microphysics scheme with prognostic cloud condensation nuclei (CCN) for weather and climate models. *Monthly Weather Review*, *138*(5), 1587–1612. https://doi.org/10.1175/2009MWR2968.1

Lin, C., Chen, D., Yang, K., & Ou, T. (2018). Impact of model resolution on simulating the water vapor transport through the Central Himalayas: Implication for models' wet bias over the Tibetan plateau. *Climate Dynamics*, *51*(9–10), 3195–3207. https://doi.org/10.1007/s00382-018-4074-x

Liu, X., Yang, M., Ou, T., Lai, H.-W., Wen, F., Dong, N., et al. (2025). Enhancing summer atmospheric water cycle simulations in the three-river headwaters region via dynamical downscaling. *Atmospheric Research*, *314*, 107810. https://doi.org/10.1016/j.atmosres.2024.107810

Liu, Z., Gao, Y., & Zhang, G. (2022). How well can a convection-permitting-modelling improve the simulation of summer precipitation diurnal cycle over the Tibetan Plateau? *Climate Dynamics*, *58*(11–12), 3121–3138. https://doi.org/10.1007/s00382-021-06090-3

Lu, J., Li, T., & Wang, L. (2021). Precipitation diurnal cycle over the maritime continent modulated by the climatological annual cycle. *Journal of Climate*, *34*(4), 1387–1402. https://doi.org/10.1175/JCLI-D-20-0130.1

Lucas-Picher, P., Argüeso, D., Brisson, E., Tramblay, Y., Berg, P., Lemonsu, A., et al. (2021). Convection-permitting modeling with regional climate models: Latest developments and next steps. *WIREs Climate Change*, *12*(6). https://doi.org/10.1002/wcc.731

Matsui, T., Zhang, S. Q., Lang, S. E., Tao, W.-K., Ichoku, C., & Peters-Lidard, C. D. (2020). Impact of radiation frequency, precipitation radiative forcing, and radiation column aggregation on convection-permitting West African monsoon simulations. *Climate Dynamics*, *55*(1–2), 193–213. https://doi.org/10.1007/s00382-018-4187-2

Mears, C., Lee, T., Ricciardulli, L., Wang, X., & Wentz, F. (2022). RSS cross-calibrated multi-platform (CCMP) 6-hourly ocean vector wind analysis on 0.25 deg grid, Version 3.0 [Dataset]. *Remote Sensing Systems (RSS) Air-Sea Essential Climate Variables (AS-ECV)*. https://doi.org/10.56236/RSS-uv6h30

Menne, M. J., Durre, I., Vose, R. S., Gleason, B. E., & Houston, T. G. (2012). An overview of the global historical climatology network-daily database [Dataset]. *Journal of Atmospheric and Oceanic Technology*, *29*(7), 897–910. https://doi.org/10.1175/JTECH-D-11-00103.1

Nguyen, P., Bador, M., Alexander, L. V., Lane, T. P., & Ngo-Duc, T. (2022). More intense daily precipitation in CORDEX-SEA regional climate models than their forcing global climate models over Southeast Asia. *International Journal of Climatology*, *42*(12), 6537–6561. https://doi.org/10.1002/joc.7619

Ohsawa, T., Ueda, H., Hayashi, T., Watanabe, A., & Matsumoto, J. (2001). Diurnal variations of convective activity and rainfall in tropical Asia. *Journal of the Meteorological Society of Japan. Series II*, *79*(1B), 333–352. https://doi.org/10.2151/jmsj.79.333

Ou, T., Chen, D., Chen, X., Lin, C., Yang, K., Lai, H.-W., & Zhang, F. (2020). Simulation of summer precipitation diurnal cycles over the Tibetan Plateau at the gray-zone grid spacing for cumulus parameterization. *Climate Dynamics*, *54*(7–8), 3525–3539. https://doi.org/10.1007/s00382-020-05181-x

Ou, T., Chen, D., Tang, J., Lin, C., Wang, X., Kukulies, J., & Lai, H.-W. (2023). Wet bias of summer precipitation in the northwestern Tibetan Plateau in ERA5 is linked to overestimated lower-level southerly wind over the plateau [Dataset]. *Climate Dynamics*, *61*(5–6), 2139–2153. https://doi.org/10.1007/s00382-023-06672-3

Park, H., Kim, G., Cha, D., Chang, E., Kim, J., Park, S., & Lee, D. (2022). Effect of a scale-aware convective parameterization scheme on the simulation of convective cells-related heavy rainfall in South Korea. *Journal of Advances in Modeling Earth Systems*, *14*(6). https://doi.org/10.1029/2021MS002696

Peng, C.-H., & Chen, X. (2024). Monsoonal MCS initiation, rainfall, and diurnal gravity waves over the Bay of Bengal: Observation and a linear model. *Journal of the Atmospheric Sciences*, *81*(8), 1401–1418. https://doi.org/10.1175/JAS-D-23-0230.1

Prein, A. F., Ban, N., Ou, T., Tang, J., Sakaguchi, K., Collier, E., et al. (2023). Towards ensemble-based kilometer-scale climate simulations over the third pole region. *Climate Dynamics*, *60*(11–12), 4055–4081. https://doi.org/10.1007/s00382-022-06543-3

Rasmussen, K. L., Prein, A. F., Rasmussen, R. M., Ikeda, K., & Liu, C. (2020). Changes in the convective population and thermodynamic environments in convection-permitting regional climate simulations over the United States. *Climate Dynamics*, *55*(1–2), 383–408. https://doi.org/10.1007/s00382-017-4000-7

Sapucci, C. R., Mayta, V. C., & da Silva Dias, P. L. (2022). Evaluation of diverse-based precipitation data over the Amazon Region. *Theoretical and Applied Climatology*, *149*(3–4), 1167–1193. https://doi.org/10.1007/s00704-022-04087-4

Sato, T., Miura, H., Satoh, M., Takayabu, Y. N., & Wang, Y. (2009). Diurnal cycle of precipitation in the tropics simulated in a global cloud-resolving model. *Journal of Climate*, *22*(18), 4809–4826. https://doi.org/10.1175/2009JCLI2890.1

Satomura, T. (2000). Diurnal variation of precipitation over the Indo-China Peninsula. *Journal of the Meteorological Society of Japan. Series II*, *78*(4), 461–475. https://doi.org/10.2151/jmsj1965.78.4_461

Schubert, D., van der Linden, R., Reyers, M., Fink, A. H., Massmeyer, K., & Pinto, J. G. (2017). Statistical-dynamical downscaling of precipitation for Vietnam: Methodology and evaluation for the recent climate. *International Journal of Climatology*, *37*(11), 4211–4228. https://doi.org/10.1002/joc.5062

Skamarock, W. C., Klemp, J. B., Dudhia, J., Gill, D. O., Barker, D., Duda, M. G., et al. (2008). A description of the advanced research WRF version 3. *(No. NCAR/TN-475+STR)*. https://doi.org/10.5065/D68S4MVH

Song, H.-J., & Sohn, B.-J. (2018). An evaluation of WRF microphysics schemes for simulating the warm-type heavy rain over the Korean Peninsula. *Asia-Pacific Journal of Atmospheric Sciences*, *54*(2), 225–236. https://doi.org/10.1007/s13143-018-0006-2

Song, J., Song, F., Feng, Z., Leung, L. R., Li, C., & Wu, L. (2024). Realistic precipitation diurnal cycle in global convection-permitting models by resolving mesoscale convective systems. *Geophysical Research Letters*, *51*(13), e2024GL109945. https://doi.org/10.1029/2024GL109945

Takayabu, I., Ishizaki, N. N., Nakaegawa, T., Sasaki, H., & Wongseree, W. (2021). Potential of representing the diurnal cycle of local-scale precipitation in Northeastern Thailand using 5-km and 2-km grid regional climate models. *Hydrological Research Letters*, *15*(1), 1–8. https://doi.org/10.3178/hrl.15.1

Tangang, F., Chung, J. X., Supari, Ngai, S. T., Salimun, E., Cruz, F., et al. (2021). Progress in climate change downscaling simulations in Southeast Asia. In *Climate resilience and environmental sustainability approaches* (pp. 13–36). Springer Singapore. https://doi.org/10.1007/978-981-16-0902-2_2

Tangang, F., Santisirisomboon, J., Juneng, L., Salimun, E., Chung, J., Supari, S., et al. (2019). Projected future changes in mean precipitation over Thailand based on multi-model regional climate simulations of CORDEX Southeast Asia. *International Journal of Climatology*, *39*(14), 5413–5436. https://doi.org/10.1002/joc.6163

Tao, C., Xie, S., Ma, H., Bechtold, P., Cui, Z., Vaillancourt, P. A., et al. (2024). Diurnal cycle of precipitation over the tropics and central United States: Intercomparison of general circulation models. *Quarterly Journal of the Royal Meteorological Society*, *150*(759), 911–936. https://doi.org/10.1002/qj.4629

Tao, C., Xie, S., Tang, S., Lee, J., Ma, H.-Y., Zhang, C., & Lin, W. (2023). Diurnal cycle of precipitation over global monsoon systems in CMIP6 simulations. *Climate Dynamics*, *60*(11–12), 3947–3968. https://doi.org/10.1007/s00382-022-06546-0

Taraphdar, S., Pauluis, O. M., Xue, L., Liu, C., Rasmussen, R., Ajayamohan, R. S., et al. (2021). WRF gray-zone simulations of precipitation over the middle-East and the UAE: Impacts of physical parameterizations and resolution. *Journal of Geophysical Research: Atmospheres*, *126*(10), e2021JD034648. https://doi.org/10.1029/2021JD034648

Tian, W., Liu, X., Wang, K., Bai, P., Liang, K., & Liu, C. (2021). Evaluation of six precipitation products in the Mekong River basin. *Atmospheric Research*, *255*, 105539. https://doi.org/10.1016/j.atmosres.2021.105539

Tran, T.-N.-D., Le, M.-H., Zhang, R., Nguyen, B. Q., Bolten, J. D., & Lakshmi, V. (2023). Robustness of gridded precipitation products for Vietnam basins using the comprehensive assessment framework of rainfall. *Atmospheric Research*, *293*, 106923. https://doi.org/10.1016/j.atmosres.2023.106923

Tsujimoto, K., Ohta, T., Aida, K., Tamakawa, K., & So Im, M. (2018). Diurnal pattern of rainfall in Cambodia: Its regional characteristics and local circulation. *Progress in Earth and Planetary Science*, *5*(1), 39. https://doi.org/10.1186/s40645-018-0192-7

Wang, W., Lu, H., Yang, D., Sothea, K., Jiao, Y., Gao, B., et al. (2016). Modelling hydrologic processes in the Mekong River basin using a distributed model driven by satellite precipitation and rain gauge observations. *PLoS One*, *11*(3), e0152229. https://doi.org/10.1371/journal.pone.0152229

Watters, D., Battaglia, A., & Allan, R. P. (2021). The diurnal cycle of precipitation according to multiple decades of global satellite observations, three CMIP6 models, and the ECMWF reanalysis. *Journal of Climate*, *34*(12), 5063–5080. https://doi.org/10.1175/JCLI-D-20-0966.1

Willetts, P. D., Marsham, J. H., Birch, C. E., Parker, D. J., Webster, S., & Petch, J. (2017). Moist convection and its upscale effects in simulations of the Indian monsoon with explicit and parametrized convection. *Quarterly Journal of the Royal Meteorological Society*, *143*(703), 1073–1085. https://doi.org/10.1002/qj.2991

Wu, C., Freychet, N., Chen, C., & Hsu, H. (2017). East Asian presummer precipitation in the CMIP5 at high versus low horizontal resolution. *International Journal of Climatology*, *37*(11), 4158–4170. https://doi.org/10.1002/joc.5055

Xiang, R., Steger, C. R., Li, S., Pellissier, L., Sørland, S. L., Willett, S. D., & Schär, C. (2024). Assessing the regional climate response to different Hengduan Mountains geometries with a high-resolution regional climate model. *Journal of Geophysical Research: Atmospheres*, *129*(6), e2023JD040208. https://doi.org/10.1029/2023JD040208

Xie, S., Wang, Y., Lin, W., Ma, H., Tang, Q., Tang, S., et al. (2019). Improved diurnal cycle of precipitation in E3SM with a revised convective triggering function. *Journal of Advances in Modeling Earth Systems*, *11*(7), 2290–2310. https://doi.org/10.1029/2019MS001702

Yang, G.-Y., & Slingo, J. (2001). The diurnal cycle in the tropics. *Monthly Weather Review*, *129*(4), 784–801. https://doi.org/10.1175/1520-0493(2001)1290784:TDCITT2.0.CO;2

Yano, J.-I., Bister, M., Fuchs, Ž., Gerard, L., Phillips, V. T. J., Barkidija, S., & Piriou, J.-M. (2013). Phenomenology of convection-parameterization closure. *Atmospheric Chemistry and Physics*, *13*(8), 4111–4131. https://doi.org/10.5194/acp-13-4111-2013

Yashiro, H., Kajikawa, Y., Miyamoto, Y., Yamaura, T., Yoshida, R., & Tomita, H. (2016). Resolution dependence of the diurnal cycle of precipitation simulated by a global cloud-system resolving model. *SOLA*, *12*, 272–276. https://doi.org/10.2151/sola.2016-053

Yatagai, A., Kamiguchi, K., Arakawa, O., Hamada, A., Yasutomi, N., & Kitoh, A. (2012). APHRODITE: Constructing a long-term daily gridded precipitation dataset for Asia based on a dense network of rain gauges [Dataset]. *Bulletin of the American Meteorological Society*, *93*(9), 1401–1415. https://doi.org/10.1175/BAMS-D-11-00122.1

Zhang, G. J. (2002). Convective quasi-equilibrium in midlatitude continental environment and its effect on convective parameterization. *Journal of Geophysical Research*, *107*(D14). https://doi.org/10.1029/2001JD001005

Zhang, L., Chen, Z., & Zhou, T. (2021). Human influence on the increasing drought risk over Southeast Asian monsoon region. *Geophysical Research Letters*, *48*(11), e2021GL093777. https://doi.org/10.1029/2021GL093777

Zhao, Y., Zhou, T., Li, P., Furtado, K., & Zou, L. (2021). Added value of a convection permitting model in simulating atmospheric water cycle over the Asian water tower. *Journal of Geophysical Research: Atmospheres*, *126*(13), e2021JD034788. https://doi.org/10.1029/2021JD034788

Zhou, W., Leung, L. R., & Lu, J. (2022). Linking large-scale double-ITCZ bias to local-scale drizzling bias in climate models. *Journal of Climate*, *35*(24), 7965–7979. https://doi.org/10.1175/JCLI-D-22-0336.1